DIPLOMARBEIT

Efficiency and Performance Studies of Depleted Monolithic Active Pixelated Particle Detectors

im Rahmen des Studiums

Physikalische Energie und Messtechnik

eingereicht von

Harald Handerkas BSc
Matrikelnummer 11915800

ausgeführt am
Atominstitut der Fakultät für Physik der Technischen Universität Wien und
dem Institut für Hochenergiephysik der Österreichischen Akademie der Wissenschaften (HEPHY)

Betreuung
Privatdoz. Dipl.-Ing. Dr.techn. Christoph Schwanda (TU Wien / Atominstitut)
Univ.Lektor Dipl.-Ing. Dr.techn. Thomas Bergauer (ÖAW / HEPHY)

Wien, 21.03.2025

(Unterschrift Verfasser/in) (Unterschrift Betreuer/in)

Abstract

Monolithic Active Pixel Sensors (MAPS) are particle detectors that combine a sensor and corresponding readout electronics in a single silicon wafer. This detector design is particularly interesting for high-energy physics since it can be fabricated with commercial CMOS technology at a lower cost compared to hybrid pixel detectors. Furthermore, the thin design allows for a low material budget, which is essential for applications such as vertex detectors in lepton colliders. This master's thesis investigates the performance of two flavors of Depleted MAPS (DMAPS) with and without radiation damage, particularly the so-called RD50-MPW4 and the TJ-Monopix2 chips. The RD50-MPW4 chip is a prototype developed by the CERN-RD50 CMOS group. Significant design works were performed in-house at HEPHY in the past. The TJ-Monopix2 chip was created to meet the requirements of the HL-LHC ATLAS ITk upgrade. It is now of particular interest to use for the Belle-II VTX upgrade.

For the performance characterization, eight samples of the RD50-MPW4 and two samples of the TJ-Monopix2 were measured at the particle accelerator facility DESY For unirradiated samples, an efficiency of 99.99 % could be achieved for the RD50-MPW4. For the unirradiated TJ-Monopix2 sample, an efficiency of 99.94 % could be reached. Reasonable performance could be measured for the RD50-MPW4 irradiated up to a fluence of $1 \times 10^{15}\,\mathrm{n_{eq}cm^{-2}}$ and for the TJ-Monopix2 irradiated up to a fluence of $5 \times 10^{14}\,\mathrm{n_{eq}cm^{-2}}$.

Acknowledgements

I would like to thank my supervisors Thomas Bergauer and Christoph Schwanda who gave me the possibility to conduct my master's thesis in the exciting field of experimental particle physics. Furthermore, I would like to express my gratitude to all HEPHY members situated at Nikolsdorfer Gasse for giving me a warm welcome in this field. I would especially like to thank Bernhard Pilsl, Maximilian Babeluk and Christian Irmler for giving me a phenomenal introduction and support throughout my thesis and the unforgettable test beam experiences.
Finally, I would like to express my special thanks to my family and friends for their support and encouragement throughout my studies.

The measurements leading to most of the results in this thesis have been performed at the Test Beam Facility at DESY Hamburg (Germany), a member of the Helmholtz Association (HGF). The research leading to the results in this thesis has received funding from the European Union's Horizon Europe research and innovation program under grant agreement no. 101057511. Furthermore, the financial support of the Austrian Ministry of Education, Science and Research is gratefully acknowledged for providing beam time and research infrastructure at MedAustron.

Contents

1. Introduction **1**
1.1. Particle Detectors in High Energy Physics Experiments 1
1.2. Belle II Experiment and VTX Upgrade 3
1.3. RD-50 Collaboration 4

2. Physical Background **5**
2.1. Interaction of particles with matter 5
2.1.1. Energy loss of heavy charged particles 6
2.1.2. Energy loss of electrons 9
2.1.3. Multiple Coulomb Scattering 10
2.2. Semiconductors 11
2.2.1. PN junction 13
2.2.2. Utilization as particle detector 15
2.3. Radiation Damage in Silicon 16
2.3.1. Doping concentration 17
2.3.2. Leakage Current 18
2.3.3. Charge Trapping 19

3. Silicon Detectors **20**
3.1. Complementary Metal-Oxide-Semiconductors 21
3.2. (Depleted) Monolithic Active Pixel Sensors 22
3.2.1. RD50-MPW4 26
3.2.2. TJ-Monopix2 27
3.3. Characterization of Detectors 30
3.3.1. Test beam 30
3.3.2. Observables 30
3.3.2.1. Time over Threshold 30
3.3.2.2. Correlations 31
3.3.2.3. Cluster Size 32
3.3.2.4. Spatial Residuals 33
3.3.2.5. Spatial Resolution 33
3.3.2.6. Efficiency 34
3.3.2.7. Timing 34
3.4. Analysis Framework 34
3.4.1. Event Building 35
3.4.2. Modules 35
3.4.2.1. Clustering 35
3.4.2.2. Tracking 35

3.4.2.3. DUTAssociation 36
3.4.2.4. Analysis 36
3.4.3. Alignment 37

4. Performance studies RD50-MPW4 38
4.1. Experimental Setup 38
4.1.1. DESY 39
4.1.2. MedAustron 39
4.2. Efficiency and Performance Measurements without radiation damage 39
4.2.1. Trade off between Efficiency and Resolution 39
4.2.2. Standard Settings 40
4.2.3. Impact of Bias Voltage and Threshold 41
4.2.3.1. ToT 42
4.2.3.2. Cluster Size 43
4.2.3.3. Efficiency as a function of Threshold 43
4.2.4. Spatial Resolution 44
4.2.5. Timing 45
4.2.6. Impact of DAC Settings 48
4.3. Characterization of irradiated samples 51
4.3.1. Cooling Setup 52
4.3.2. Observed Impact of Radiation Damage 52
4.3.3. Bias Voltage Scans 53
4.3.3.1. Efficiency 53
4.3.3.2. ToT 54
4.3.3.3. Cluster Size 55
4.3.3.4. Spatial Resolution 55
4.3.3.5. Bias Voltage Characteristics 56
4.3.3.6. Timing 57
4.3.4. VNFB DAC Scans with Irradiated Samples 58
4.3.4.1. ToT 59
4.3.4.2. Cluster Size 60
4.3.4.3. Spatial resolution 61

5. TJ-Monopix2 63
5.1. Lab Measurements 63
5.1.1. Power Consumption Measurements 63
5.1.1.1. Clock frequency and BCID 63
5.1.1.2. IBIAS 64
5.1.1.3. Occupancy and VPC 65
5.1.2. Temperature Calibration 66

5.2. Efficiency and Performance Measurements 68
5.2.1. Test Beam Setup 68
5.2.2. Performance without Irradiation 69
5.2.3. Impact of Proton Irradiation 70
5.2.4. Temperature measurements 71

6. Operation Settings 73

7. Conclusion 74
7.1. RD50-MPW4 74
7.2. TJ-Monopix2 75

Bibliography i

List of Figures v

List of Tables viii

Acronyms ix

A. Appendix xii
A.1. Corryvreckan detectors file xii
A.2. Corryvreckan config file xv

1. Introduction

In the following chapter, a brief introduction to particle detectors in high energy physics together with the example of the Belle II experiment [1] and the RD-50 collaboration [2] are given in order to motivate current developments for silicon sensors based on Complementary Metal-Oxide-Semiconductors (CMOS) technology. In chapter 2, chosen physical concepts are described which are needed for the practical part of this thesis. Chapter 3 focuses on silicon detectors and contains a description of the two detectors RD50-MPW4 and TJ-Monopix2 which were studied throughout this thesis. Furthermore, a description of the analysis of test beam data is given within this section. Chapter 4 and 5 contain the results of test beam data for irradiated and unirradiated samples of each detector type.

1.1. Particle Detectors in High Energy Physics Experiments

Particle detectors in high energy physics (HEP) experiments are built around a collision point and consist of several layers fulfilling different tasks. The design can vary depending on the colliding particle types and the objective of the experiment. A typical structure of the layout of the different detector systems is depicted in fig.1. Their tasks are described below.

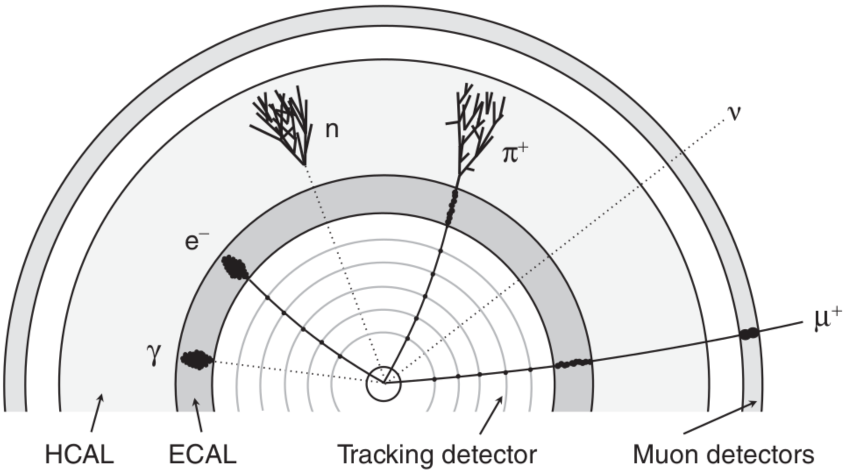

Figure 1: Schematic of a collider experiment and the interaction of different particle types with different detector systems. HCAL/ECAL: hadronic/electromagnetic calorimeter. [3]

Tracking
One of the inner detector systems of a collider experiment is the tracking detector which reconstructs the trajectories of passing particles. This process is called tracking. The tracking process can be divided into track finding, where hits on different detector layers are associated to a single particle and a fitting process where the trajectory is reconstructed with the hit information from the track finding. After the track fitting, an assessment of the track quality using statistical methods is necessary. In the collider detector, a magnetic field is applied, causing charged particles to follow a curved trajectory. The curvature of the trajectories allows reconstructing the momentum of the particles and the direction of deflection allows determining the sign of its charge. [4, 5]

Vertexing
The detector system which is closest to the interaction point is used to reconstruct primary vertices and further vertices of higher order. In high-luminosity collider experiments, many collisions occur at a single bunch crossing, resulting in many initial interaction points called primary vertices. However, it is statistically almost certain that only one of them is of potential physical interest and activates the trigger. The aim of vertexing is to find a set of particles produced by the so called signal vertex which activated the trigger and estimate its position. Particles with short life times can decay and produce further particles before reaching the first detector layer. The trajectories of the produced daughter particles can be used to reconstruct the point where the decay took place which is referred to as secondary vertex. Vertexing needs detector systems with low occupancy in order to avoid multiple hits which lead to problems in the event reconstruction. Furthermore, vertexing algorithms depend on low spatial and timing resolution in order to reconstruct the vertices accurately. Due to the close distance to the collision point of this detector system, it has to cope with a high background particle fluence resulting in radiation damage. [4, 5]

Calorimetry
Calorimeters measure the energy of high-energetic particles. Since it is a destructive measurement, it has to be located after the tracking layer. A particle hitting the calorimeter leads to a chain of inelastic reactions that produce further particles resulting in a particle shower in the detector. The energy of the initial particle is measured via the deposited charge in the detector, scintillator light or Cherenkov light. Calorimeters can be distinguished between electromagnetic calorimeters for electrons, positrons and photons and hadronic calorimeters for hadrons. [6]

This thesis deals with two detectors designed for tracking and vertexing. In the following section an overview of the vertex detector of the Belle II experiment is given as example for their usage in HEP experiments.

1.2. Belle II Experiment and VTX Upgrade

The Belle II experiment [1] is located at the SuperKEKB accelerator [7] in Tsukuba, Japan. It is an asymmetric collider for electrons at energies of 7 GeV and positrons at 4 GeV. The objective of the Belle II experiment is to investigate new weak interactions in the flavor section beyond the standard model. An overview of the detector systems is depicted in fig.2. [8]

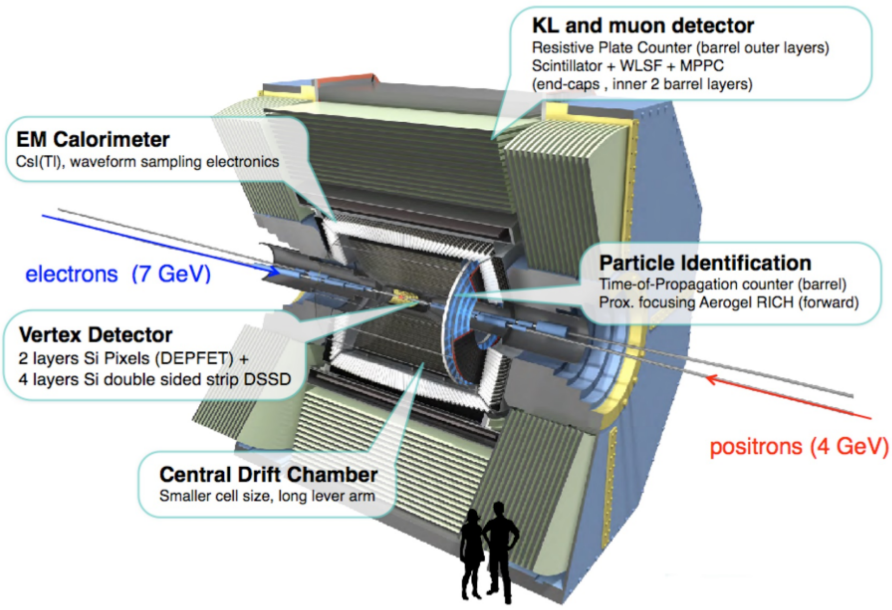

Figure 2: Schematic overview of the detector systems of the Belle II experiment. [8]

Currently, the Belle II vertex detector (VXD) consists of two different systems. The two innermost layers are made of pixel sensors based on depleted p-channel field effect transistor (DEPFET) technology. These two layers are referred to as the Pixel Detector (PXD). The PXD is surrounded by four layers of Double-Sided Silicon micro-strip Detectors (DSSDs) called Silicon Vertex Detector (SVD). [1]

For the VXD, an upgrade is planned for the next long shutdown which is scheduled to take place after 2032. A fixed year has not yet been announced, depending on the final plans for the upgrade. For the VXD upgrade, a CMOS based structure is considered as the most promising solution. It should increase the robustness against the machine background and allow better reconstruction for low momentum particles and improve the vertex resolution. Current design approaches are made of five or six layers of the Optimised Belle II monolithic pixel (OBELIX) sensor [9] currently under development. The design of OBELIX is based on the TJ-Monopix2. [10]

1.3. RD-50 Collaboration

In the *ECFA Detector Research and Development Roadmap* from 2021 [11], solid state detectors are mentioned to play a key role in measuring primary and secondary vertices and tracking charged particles in future collider experiments. The roadmap describes four different detector R&D themes (DRDT). DRDT 3.1 describes the full integration of sensing and microelectronics in monolithic CMOS pixel sensors and DRDT 3.3 describes the extension of solid state sensors to operate at extreme fluences. For monolithic active pixel sensors for small-pixel trackers, a radiation tolerance from $10^{15}\,\mathrm{n_{eq}cm^{-2}}$ to $10^{16}\,\mathrm{n_{eq}cm^{-2}}$ is set as goal. [11]

The RD50 Collaboration [2] is a CERN R&D collaboration dedicated to the development of radiation hard silicon devices for high luminosity collider experiments. The latest developed chip by this collaboration is the RD50-MPW4 which is a depleted monolithic active pixel sensor (see sec.3.2) following the HV-CMOS approach. Compared to its predecessor, the RD50-MPW3, the RD50-MPW4 has separated digital power and ground domains of the pixel matrix and periphery. This design improvement was necessary in order to reduce noise coupling from the digital readout periphery with the pixel matrix. Furthermore, the guard ring structure of the RD50-MPW4 got improved based on the guard ring structure of a monolithic CMOS detector prototype LF-Monopix2 allowing to apply a bias voltage higher than 300 V. [12, 13]

2. Physical Background

2.1. Interaction of particles with matter

For the description of the interaction of particles with matter, the concept of the cross section is needed. The cross section σ is used to determine the probability of a particle reaction. It can be illustrated as the effective area of a target particle, in which it can interact with an incoming one. An illustration for a fixed target experiment is given in fig.3 with the test volume S filled with N_T target particles and thickness l.

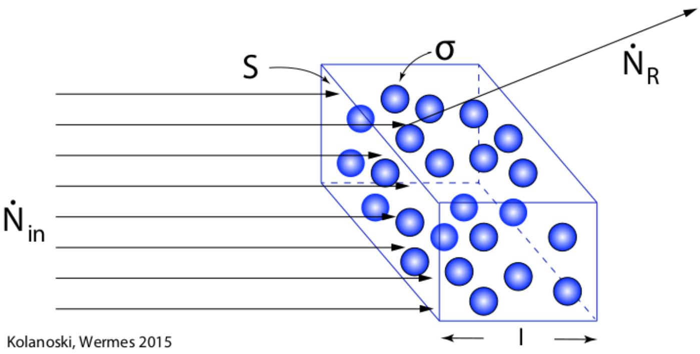

Figure 3: Scheme of the concept of the cross section. $\dot{N}_R$ and $\dot{N}_{in}$ refer to the reaction rate and incoming particle rate. [6]

The energy loss ΔE of a charged particle passing through a material with the thickness Δx is a statistical process. It is the result of the sum of small energy losses δE_n (see eq.1) due to excitation and ionization processes. [6]

$$\Delta E = \sum_{n=1}^{N} \delta E_n \tag{1}$$

Statistical fluctuations occur for the single energy losses δE_n as well as for the number of interactions N. For a fixed Δx, a probability density for ΔE can be defined (eq.2). Due to the central limit theorem of statistics, this distribution becomes normally distributed for infinite N since δE_n is statistically independent to ΔE.

$$\int_{\Delta E_{min}}^{\Delta E_{max}} f(\Delta E, \Delta x) d(\Delta E) = 1 \tag{2}$$

For thin detectors, the central limit theorem of statistics is not fulfilled, resulting in an asymmetric distribution called Landau distribution $f_L(\lambda)$ (eq.3) which is depicted in fig.4. Its moments are not defined due to the infinite long tail. However, the Landau distribution has a maximum at λ = -0.22278 which can be used to define a most probable value instead. The energy loss is included in the parameter λ. [6]

$$f_L(\lambda) = \frac{1}{\pi} \int_0^{\infty} e^{-t \ln t - \lambda t} \sin(\pi t) dt \tag{3}$$

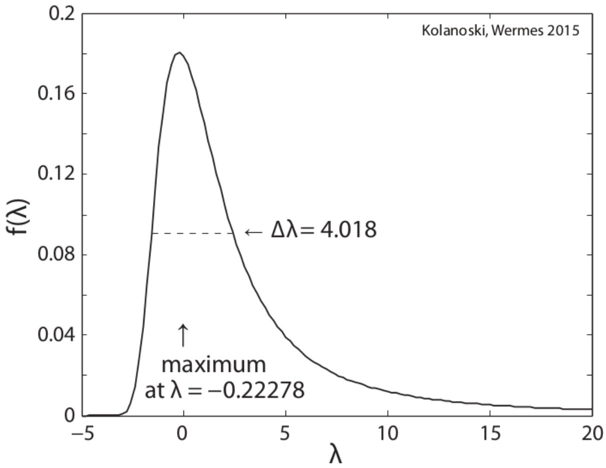

Figure 4: Landau distribution as described in eq.3 for thin detectors [6].

2.1.1. Energy loss of heavy charged particles

The mean energy loss of a charged particle per unit length can be calculated with the differential cross section $\frac{d\sigma}{dT}$ where T is the kinetic energy, β the relativistic velocity, n the target number density and M the mass of the incoming particle as shown in eq.4. [6]

$$-\langle\frac{dE}{dx}\rangle = n\int_{T_{min}}^{T_{max}} T\frac{d\sigma}{dT}(M,\beta,T)dT \tag{4}$$

For heavy charged particles, which excludes electrons and positrons, the result of the expression above, extended with two correction terms, is the Bethe-Bloch formula (eq.5). The average energy loss is also referred to as stopping power, since it describes the range of how deep charged particles can penetrate a material. [6]

$$-\langle\frac{dE}{dx}\rangle = K\frac{Z}{A}\rho\frac{z^2}{\beta^2}\left[\frac{1}{2}\ln\frac{2m_ec^2\beta^2\gamma^2T_{max}}{I^2} - \beta^2 - \frac{\delta(\beta\gamma)}{2} - \frac{C(\beta\gamma,I)}{Z}\right] \tag{5}$$

$K = 4\pi N_A r_e^2 m_e c^2$	
z, β	particle charge
$\beta = \frac{v}{c}$	relativistic velocity
Z	atomic number of medium
A	atomic mass of medium
δ	density correction
$\frac{C}{Z}$	shell correction
I	mean excitation energy

Figure 5 shows the mean energy loss per unit length over $\beta\gamma$. The plot shows a low energy region following a $\frac{1}{\beta^2}$ behavior and a high energy region with a behavior of $ln(\gamma) + const$. Between these regions there is a minimum around $\beta\gamma \approx 3.5$. Particles near this minimum are referred as minimum-ionizing particle (MIP). [6]

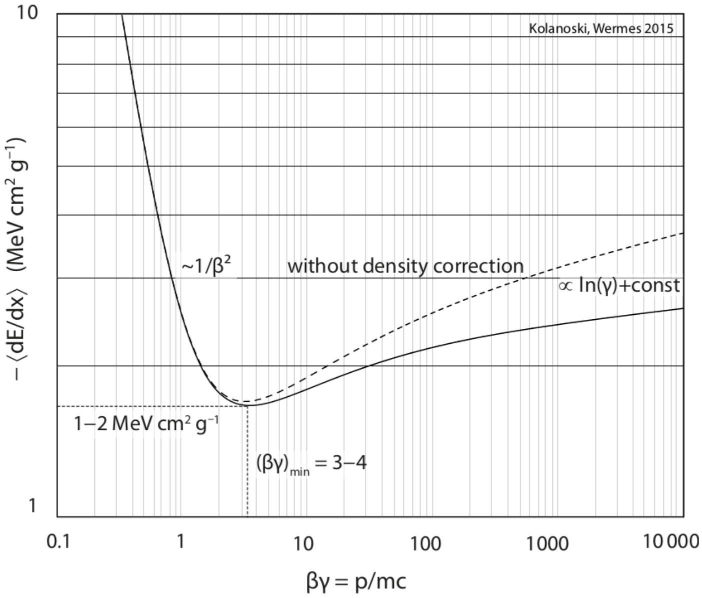

Figure 5: Mean energy loss of charged pions in silicon showing the dependence on $\frac{1}{\beta^2}$ for low energies and $ln(\gamma) + const$ for higher energies. [6]

For low energies, the $\frac{1}{\beta^2}$ behavior leads to a high energy loss within a short distance towards the end of the particle's path (see fig.6). This energy deposition is called *Bragg peak* and is used for radiation therapy of deep lying tumors. [6]

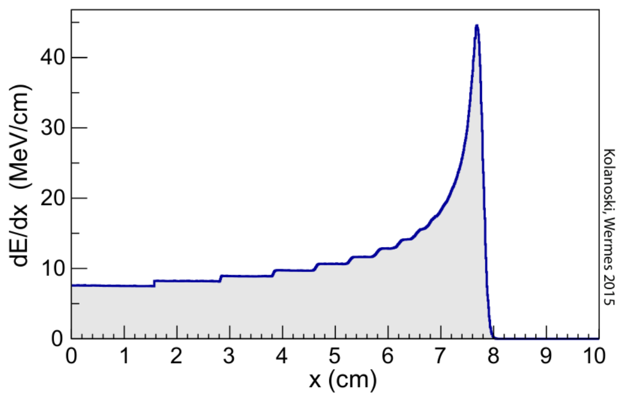

Figure 6: Simulation of energy loss per path length for 100 MeV protons in water illustrating the Bragg peak. [6]

Density Correction
At high energies, the electric field flattens and extends transversely due to relativistic effects. This transformation of the electric field increases the distant-collision contribution and leads to a term proportional to $\ln(\beta\gamma)$. In real media, the field extension is limited due to polarization, which leads to a correction term $\delta(\beta\gamma)$ called density correction. [14]

Shell Correction
The $\frac{1}{\beta^2}$ dependency for low energies can be motivated with the proportionality between momentum transfer Δp and interaction time Δt. The interaction time is defined as stated in eq.6 with the impact parameter b.

$$\Delta t = \frac{b}{\gamma v} \quad \text{and} \quad \Delta p \quad \alpha \quad \Delta t \tag{6}$$

Inserting these relations to the energy and momentum relationship, the following dependency for the transferred energy follows as shown in eq.7.

$$\begin{aligned} \Delta E = \frac{\Delta p^2}{2m} \quad &\alpha \quad \frac{b^2}{\gamma^2 v^2} \\ \text{with} \quad \beta &= \frac{v}{c} \\ \Rightarrow \Delta E \quad &\alpha \quad \frac{1}{\beta^2} \end{aligned} \tag{7}$$

This behavior is only valid until the particles reach velocities which are in the range of the velocities of shell electrons. In this case, further interactions have to be considered which have been neglected so far, leading to the introduction of a shell correction term $\frac{C}{Z}$. [6]

2.1.2. Energy loss of electrons

Bremsstrahlung describes the emitted energy per unit time from an accelerated charge and is formulated in classical electrodynamics as shown in eq.8 in general and for a decelerated particle in the field of a nucleus [6].

$$\frac{dW}{dt} = \frac{2}{3}\frac{z^2 e^2}{4\pi\epsilon_0 c^3} \mid \ddot{x} \mid^2 \quad \alpha \quad \frac{z^4 Z^2 e^6}{m^2} \tag{8}$$

The main difference between the energy loss of electrons and heavy charged particles is the difference in mass. For electrons, Bremsstrahlung has to be considered, which is an effect that can be neglected for particles with higher mass (see eq.8). For high-energy electrons, this effect is the dominant mechanism for energy loss in matter. A characteristic value for this effect is the radiation length (X_0). It is defined as the mean distance over which a high-energy electron loses all but $\frac{1}{e}$ of its energy by Bremsstrahlung. The rate of the energy loss of electrons in matter due to Bremsstrahlung is nearly proportional to its energy while its ionization loss rate depends on the logarithm of the energy. This allows to define a critical energy E_c which is given by the energy, at which the rate of energy-losses of both effects are equal. [14]

2.1.3. Multiple Coulomb Scattering

Charged particles passing through a medium are deflected by scattering due to interactions with the Coulomb field of the nuclei. At energies $E >> m_e c^2$, the impact of interactions with shell electrons can be neglected [6]. The scattering process with a single nucleus can be described by the Rutherford cross section (eq.9). It depends on the charge z, the velocity β, the momentum p and the scattered angle θ of the scattered particle as well as on the charge of the nucleus Z. [6]

$$\frac{d\sigma}{d\Omega}\mid_{Rutherford} = z^2 Z^2 \alpha^2 \hbar^2 \frac{1}{\beta^2 p^2} \frac{1}{4\sin\left(\frac{\theta}{2}\right)} \tag{9}$$

If a medium is thick enough to scatter a traversing particle more than about 20 times, the scattering can be described by Molière theory. The obtained distribution by the Molière theory can be approximated by a Gaussian distribution for a large amount of scatters due to the central limit theorem of statistics. The scattering can be characterized by θ_{ms} which is the standard deviation of the angle θ_{plane} (see fig.7). It can be approximated as shown in eq.10 with $E_s = m_e c^2 \sqrt{\frac{4\pi}{\alpha}}$, α being the fine-structure constant, the thickness of the scattering material x and the radiation length X_0. [6]

$$\theta_{ms} \approx \frac{E_s}{\sqrt{2} pc\beta} \sqrt{\frac{x}{X_0}} \tag{10}$$

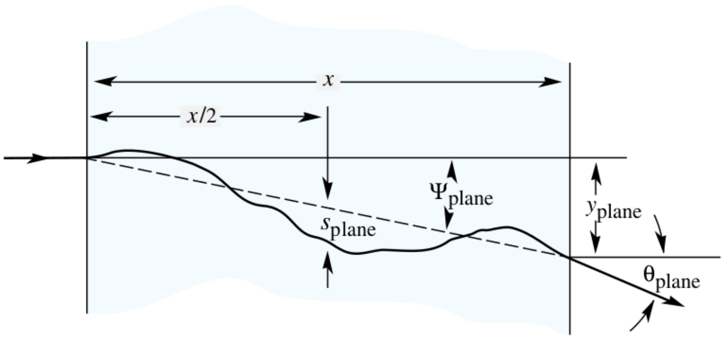

Figure 7: Illustration of the trajectory resulting from multiple Coulomb scattering and the deflection angle θ_{plane}. [14]

2.2. Semiconductors

The dense periodic crystal structure of solids leads to energy level structures which are called energy bands. The highest band is called conduction band and the band underneath it valence band. These two bands are separated by a band gap. The size of the band gap and the location of the conduction and valence band depend on the material and define the conduction properties. For insulators, the band gap is large with a value about 9 eV. In contrast, for conductors, the conduction band overlaps with the valence band. Also a partially filled conduction band leads to conducting behavior. If the band gap is in the range of about 1 eV (1.2 eV for Si at room temperature), the material is categorized as a semiconductor. In that case, electrons can enter the conduction band from the valence band via thermal excitation or via an external electrical field. This process generates negative charge in the nearly empty conduction band and leaves a hole in the valence band which enables current flow. These four cases are depicted in fig.8. [6]

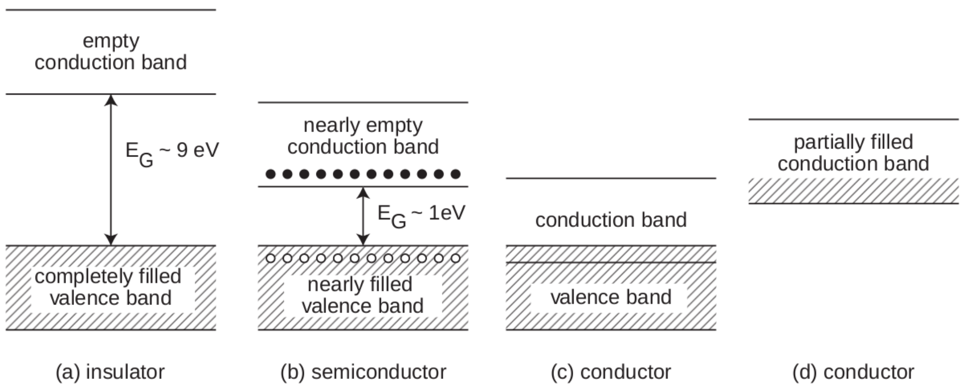

Figure 8: Conduction behavior of materials depending on the band gap E_G for insulators (a) semiconductors (b) and conductors (c,d). [6]

For detectors, silicon (Si) is the mostly used semiconductor. Other examples of semiconductors are germanium (Ge), gallium arsenide (GaAs) and cadmium telluride (CdTe). The crystal lattice of silicon has a diamond structure. A scheme of a primitive cell is shown in fig.9. Each atom has a covalent binding to four neighbors with a lattice spacing of 5.43 Å. [6]

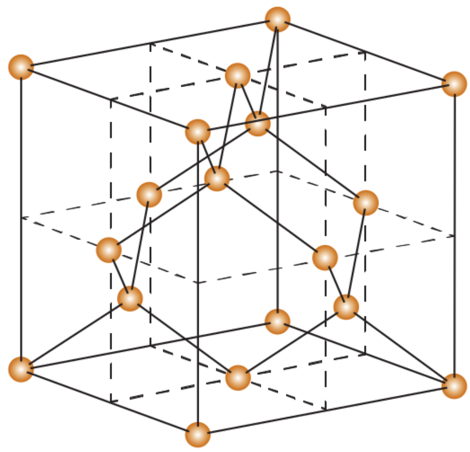

Figure 9: Primitive cell of a diamond lattice (eg. Si). [6]

The charge carrier concentration $n(E)$ in thermal equilibrium can be derived with the density of states $Z(E)$ and their occupation probability $f(E)$.

$$n(E)dE = Z(E)f(E)dE \tag{11}$$

For spin $\frac{1}{2}$ particles, the occupation probability follows a Fermi-Dirac distribution. This distribution defines the Fermi Energy E_f as the energy, where the occupation probability is equal to $\frac{1}{2}$. The Fermi-Dirac distribution can be approximated with a Boltzmann distribution if the Fermi Energy is approximately in the middle of the band gap (eq.12).

$$f_n(E) = \frac{1}{e^{\frac{E-E_f}{kT}} + 1} \approx e^{-\frac{E-E_f}{kT}} \quad \text{for} \quad (E - E_f >> kT) \tag{12}$$

The resulting number densities are given in eq.13 for electrons (n) in the conduction band and in eq.14 for holes (h) in the valence band. The values N_C and N_V give the effective densities of states in the respective band. For silicon at 300K, these are $N_C \approx 3.05 \times 10^{19}\,\mathrm{cm}^{-3}$ and $N_V \approx 2.55 \times 10^{19}\,\mathrm{cm}^{-3}$. [6]

$$n = N_C \cdot e^{-\frac{E_C - E_F}{kT}} \tag{13}$$

$$h = N_V \cdot e^{-\frac{E_F - E_V}{kT}} \tag{14}$$

2.2.1. PN junction

Extrinsic semiconductors have added impurity atoms in the substrate (Si, Ge) which change the conduction properties. These can either be donors (n-doping) which lead to an excess of conduction electrons or acceptors (p-doping) which lead to an excess of holes in the valence band. Doping changes the available number of charge carrier types and therefore changes the conduction properties. Depending on the doping, either the electrons in the conduction band or the holes in the valence band become the majority or minority charge carriers.

In doped semiconductors, the added impurities create new states which shift the Fermi-Energy closer to the energy of the conduction band for n-doping or closer to the valence band for p-doping. If n- and p-doped semiconductors are brought into direct contact, the electrons in the conduction band and holes in the valence band drift to the other region. This happens due to the concentration gradients resulting in a diffusion current I_{diff}. This process leads to a region at the boundary of the two materials called depletion zone which has no free charge carriers. The atomic cores in the depletion zone remain ionized leading to a space charge in the depletion zone. The space charge causes an intrinsic electric field which leads to a drift current which is directed in the opposite direction of the diffusion current (see fig.10). These currents are in equilibrium if no external potential is applied. The resulting built-in voltage V_{bi} for silicon in about 0.6 V. [6]

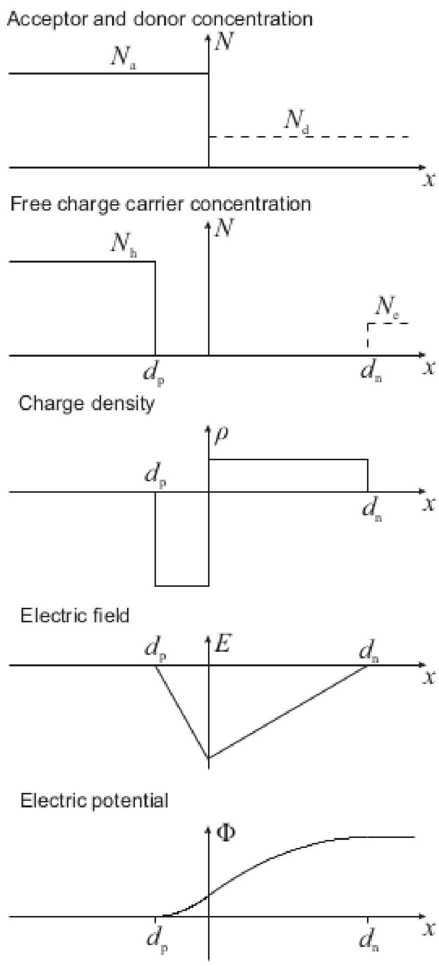

Figure 10: Model of a p-n junction. [4]

The size d of the resulting depletion zone can be approximated with eq.15 with

N_D being the doping concentration. It depends on the built-in voltage and can be changed by applying an external potential V_{ext}.

$$d \approx \sqrt{\frac{2\epsilon\epsilon_0}{e} V_{bi} \frac{1}{N_D}} \quad \text{biasing:} \quad V_{bi} \Rightarrow V_{bi} - V_{ext} \tag{15}$$

Applying an external potential leads to a non equilibrium state of the system and diffusion and drift currents are no longer equal. If the potential (V $>$ 0) is applied at the p side, the junction is forward biased and the drift current reduces compared to the diffusion current leading to a thinner depletion zone. If the junction is backward biased (V_{ext}<0 at p), the diffusion current increases leading to a wider depletion zone compared to the equilibrium state. [6]

2.2.2. Utilization as particle detector

The principle of particle detection with semiconductors is that intersecting particles transfer energy to the semiconductor which creates electron hole pairs. These free charge carriers can lead to a current which can be measured. In order to avoid recombination processes of the produced pairs, additional free charge carriers in the semiconductor have to be avoided. This makes the depletion zone the sensitive detection volume of the semiconductor. Through reverse biasing, the detection volume can be increased and the drift of the electron hole pairs is prompted by the electric field. For full depleted detectors, the drift velocity v_D can be described by the Drude model (eq.16) which depends on the mobility μ and the electric field E. Spatially sensitive silicon detectors have a drift velocity around 50 µm/ns with a thickness between 200 to 300 µm resulting in a drift time distribution of 4 to 6 ns depending on the position of the ionization. The amount of produced electron hole pairs e/h depends on the thickness of the detector d, the energy needed on average to produce a pair w_i and the particle's average energy loss which follows a Landau distribution (eq.17). At 300 K, the most probable value of produced pairs is 23 000 e/h in a 300 µm thick silicon detector for a minimum ionizing particle. [6]

$$v_D = \mu(E)E \tag{16}$$

$$e/h = \left\langle \frac{dE}{dx} \right\rangle \frac{d}{w_i} \tag{17}$$

2.3. Radiation Damage in Silicon

Radiation damage and its impact on detectors is of interest for detectors in HEP since they are permanently exposed to radiation in collider experiments. When radiation passes through detectors, it interacts with the detector, changing its material properties. As a result, the performance of detectors changes over their usage time.

The main effect of radiation damage in silicon is a damage of the crystal lattice. For charged particles, the damage occurs due to Coulomb scattering while neutrons interact via the strong force. An interaction with a silicon atom can knock it out of the lattice and create a vacancy. The removed atom can kick out further silicon atoms and create a cluster of damages. The atoms end up in an interstitial state in the lattice. These defects are impurities in the silicon bulk and can change its physical properties by creating further states in the band gap. Figure 11 shows three different possible states with respect to the band gap. [4]

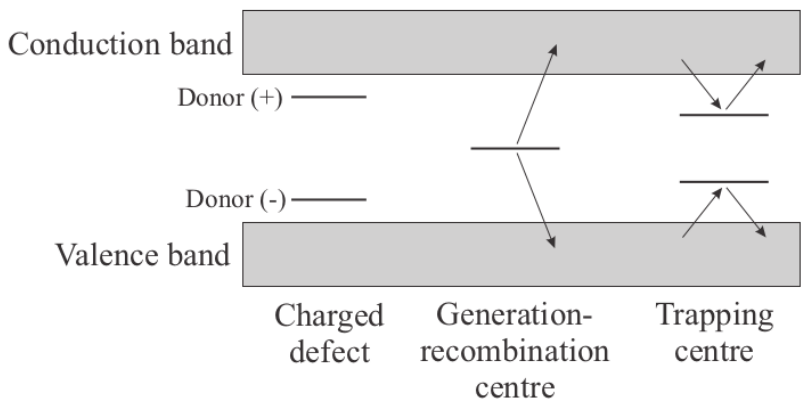

Figure 11: Possible new generated states due to impurities resulting from radiation damage in silicon. [4]

The non-ionizing energy loss (NIEL) hypothesis states, that all lattice radiation damage in silicon scales linearly with the non-ionizing energy loss. NIEL can be calculated as shown in eq.18 with N_A being the Avogadro number and A being the atomic mass. $D(E)$ is the damage function which depends on the energy and particle type. The NIEL hypothesis is a first order description of the observed damage and is suitable to describe the leakage current generation due to NIEL damage. In order to normalize the damage caused by different particle types, it is referred to the amount of damage a 1 MeV neutron would cause. This value is called equivalent fluence and is given in neutron equivalent per square centimeter ($\mathrm{n_{eq}cm^{-2}}$). [6]

$$\frac{dE}{dx}|_{NIEL}(E) = \frac{N_A}{A} D(E) \tag{18}$$

2.3.1. Doping concentration

The effective doping concentration which can also be considered as the effective space charge concentration in the silicon bulk changes due to radiation damage. Radiation damage can either affect the doping atoms directly or create charged defects as shown in fig.11. Vacancies can interact with donor atoms and deactivate them while interstitial acceptor atoms can interact with oxygen. The effects on the doping concentration depend on the fluence and also type inversion from n-type to p-type is possible (fig.12). The dominant mechanism for this are acceptor-like defects which trap free electrons from the conduction band and therefore act as p-doping. From the change of the effective space charge concentration in the depletion zone follows a dependency of the full depletion voltage of a sensor on the fluence. [6]

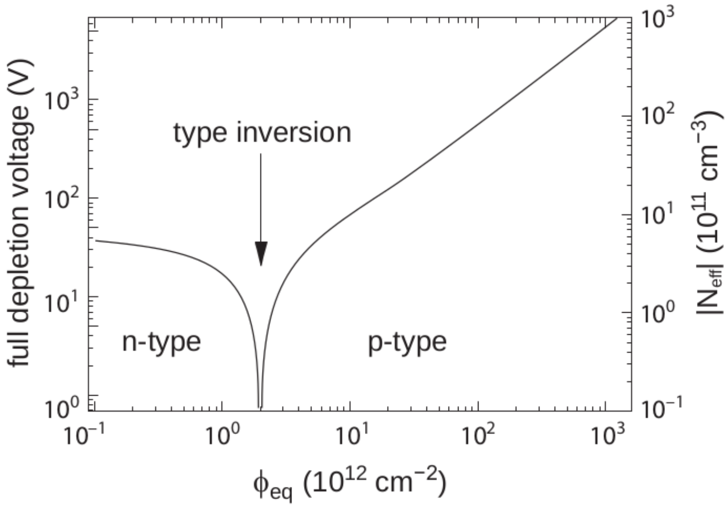

Figure 12: Full depletion voltage and effective charge carrier concentration as a function of the equivalent fluence illustrating type inversion. [6]

2.3.2. Leakage Current

Defects resulting in a state in the middle of the band gap are centers for generation and recombination of electron hole pairs. If free carriers are neglected (no recombination), the generation rate for a single defect is given by eq.19 with the emission probabilities e_n and e_p. The emission probabilities depend exponentially on the energy difference between the intrinsic Fermi energy and the energy of the defect state. [6]

$$G_t = \frac{e_n e_p}{e_n + e_p} \tag{19}$$

The sum of the generated electron hole pairs multiplied by the volume V covered by an electrode and charge is defined as leakage current I_L (eq.20).

$$I_L = eV \sum_{defects} G_t \tag{20}$$

2.3.3. Charge Trapping

Free charge carriers can be captured by trapping levels resulting from radiation damage which leads to a loss of signal. If the thermal velocity v_{th} is large compared to the drift velocity, the signal decreases exponentially with the average trapping time τ_{eff} (eq.21). In general, the impact of charge trapping on electrons is less than on holes due to their higher mobility which results in shorter drift times [4].

$$Q(t) = Q_0 e^{-\frac{t}{\tau_{eff}}} \tag{21}$$

The average trapping time can be written as a sum over all traps as shown in eq.22 with the trap concentration N, the occupation probability P of a trap and the capture cross-section σ.

$$\frac{1}{\tau_{eff}} = \sum_k N_k (1 - P_k) \sigma_k v_{th} \tag{22}$$

The trap concentration resulting from irradiation can be described with introduction rate g, the equivalence fluence Φ_{eq} and an exponential function f(t) considering trap annealing (eq.23). This model neglects trap interaction with each other, which would need a more general model including Φ^2 terms.

$$N_k = g_k \Phi_{eq} f_k(t) \tag{23}$$

For experiments, the quantities needed for the average trap time can be parameterized with the parameter β which depends on the temperature and time (eq.24) resulting in a linear dependance of the average trapping time on the equivalence fluence. [15]

$$\frac{1}{\tau_{eff}} = \beta(t, T) \Phi_{eq} \tag{24}$$

3. Silicon Detectors

Due to the higher density of solids compared to gases, charged particles can deposit a higher charge in them compared to gas based detectors, resulting in a higher signal. In order to collect the ionization signal efficiently, the material must allow the deposited charge to be mobile and avoid charge trapping. Semiconductors, especially silicon, fulfill these requirements. Silicon detectors can be realized in different design approaches.

Strip Detectors

Strip detectors consist of several strips with a width in the order of 100 µm and a length of several cm which limits the obtained information to one dimension. The wedge bonding of the strips leads to a minimum pitch in the magnitude of about 50 µm limiting the spatial resolution. In order to use strip detectors for position measurements in two dimensions, two detectors have to be combined which are rotated with respect to each other. For more than one hit at a time, this can lead to so called ghost hits illustrated in fig.13. [4]

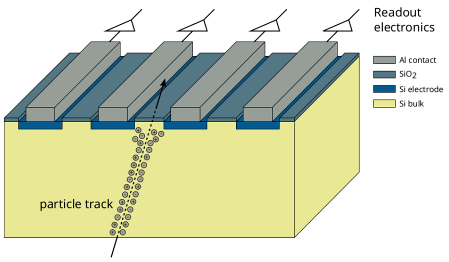

(a) Scheme of a strip detector [16]

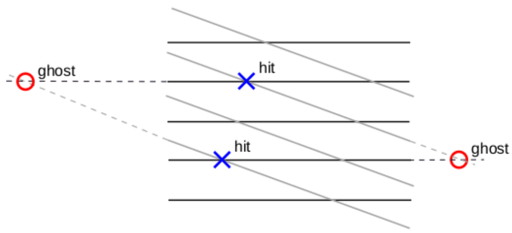

(b) Position measurement [4]

Figure 13: a) Scheme of a strip detector and b) its utilization with two rotated planes for position measurements in two dimensions.

Pixel Detectors

Pixel detectors are based on a matrix of pixels which allows better spatial resolution and better performance for high track densities due to the smaller size of the pixels compared to strips. One of the main challenges of pixel detectors is to connect the silicon sensor with the readout electronics because of the high amount of pixels. Hybrid pixel detectors consist of a separate silicon sensor connected to readout chips via bump bonds (fig.14). Bump bonding is an expensive process and the bonds are at risk of failure due to thermal stress when operated in a cooled environment. Monolithic active pixel sensors (MAPS) follow the approach of including the analog readout directly into the pixels of the sensor. MAPS are usually based on the CMOS technology described in the next chapter. [4]

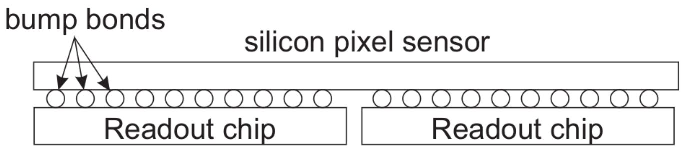

Figure 14: Scheme of the hybrid pixel detector approach separating the readout chip from the silicon sensor. [4]

3.1. Complementary Metal-Oxide-Semiconductors

CMOS stands for complementary metal-oxide-semiconductors and is the dominant fabrication process for fabricating integrated circuits. It uses p- and n-channel field effect transistors (PMOS/NMOS). Silicon is mostly used as basis material. One of the advantages of the CMOS process is that the transistors can be scaled down in size with improving fabrication technologies. [17]

A scheme of a NMOS transistor is depicted in fig.15. It consists of two n-doped regions called source and drain (highest potential) in a p-doped substrate. An electrode is located above the connection between the two terminals. If a positive potential is applied to the gate, positive charge carriers in the p substrate are repelled and a channel between source and drain for electrons forms which allows a current to flow between the terminals. The working principle for a PMOS transistor is the same with complementary doping of the substrate and terminals. [17]

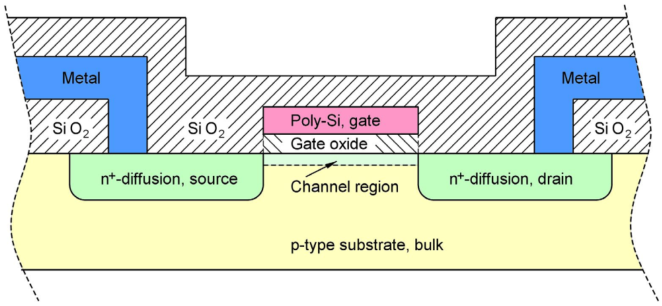

Figure 15: Cross-section of a NMOS transistor. Metal connection to gate not depicted. [17]

A CMOS structure consists of one or more PMOS and NMOS transistors (fig.16). In order to ensure the correct doping of the substrate for the PMOS transistor, it is placed in a n-doped structure called n-well which leads to a fourth terminal called bulk. This well can cover a single or several PMOS transistors. It is also possible to implement p-wells and n-wells separated by insulating layers with twin-well technologies. Compared to fig.16, the p-type substrate can be replaced with an epitaxial layer and the NMOS transistor can be embedded in a p-type well for these technologies. [17]

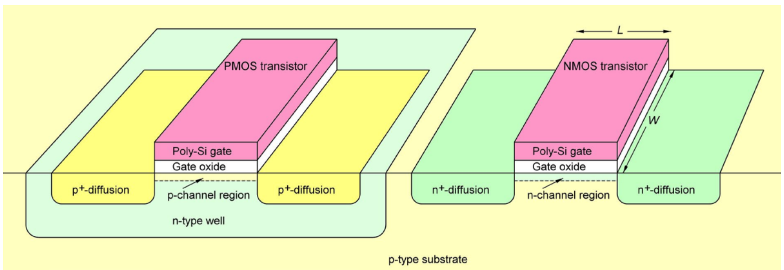

Figure 16: Scheme of a CMOS device structure consisting of a PMOS and NMOS transistor. [17]

3.2. (Depleted) Monolithic Active Pixel Sensors

MAPS are sensors which are based on CMOS technology. The electronic circuitry as well as the sensor are integrated in a single pixel which does not need bump bonding in comparison to hybrid pixel detectors. Furthermore, MAPS have a lower material budget due to their thinner layout. The material budget is the thickness x of a detector divided by its radiation length ($\frac{x}{X_0}$). Detectors with a high material budget absorb more energy and therefore can collect more signal from traversing particles, but they have more impact on the further trajectory compared to detectors with low material budget due to scattering effects and energy absorption. Their working principle is depicted in fig.17. An intersecting particle produces free electrons in the sensor which can be collected by a collection electrode (n well). Other competing n wells from PMOS transistors have to be shielded by deep p wells. The electrons in MAPS are mainly collected by unidirectional diffusion which only allows to collect a fraction of the produced free electrons which have a diffusion time in the order of 100 ns. [6]

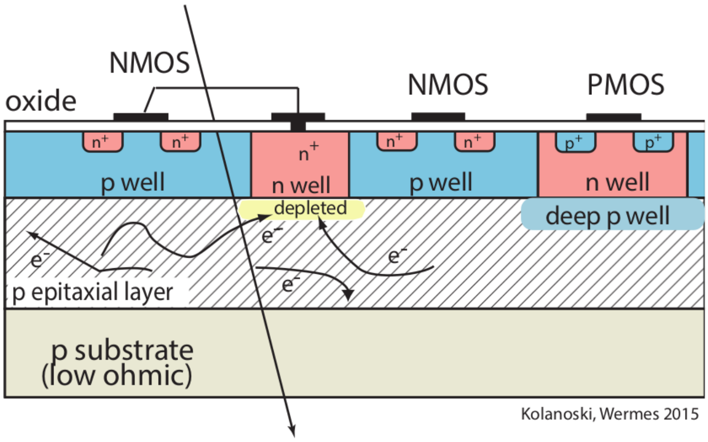

Figure 17: Scheme of the working principle of a MAPS [6]

For the application in high energy physics, a faster and complete collection of the deposited charge is beneficial in order to cope with higher rates and radiation damage. This can be achieved by collecting the charge via drift in an electric field rather than by diffusion. The depth of the depletion zone depends on the resistivity and applied external potential ($d \quad \alpha \quad \sqrt{\rho V}$). By applying an external potential, the depletion zone of the collection electrode can be increased leading to a drift governed charge collection. These detector type is called monolithic active pixel sensor (DMAPS). DMAPS can be divided into two different design approaches: large and small collection electrode design.

Large collection electrode
The large collection electrode design is realized with a deep N well containing the CMOS circuits (fig18). The depletion zone can either be created from the top surface only or if backside processing is applied to the sensor also from the deep n well to the backside. Due to the short average drift times from the deposited charge to the collection electrode, this design is considered as radiation tolerant. A disadvantage of this design is the large amplifier input capacity (about 100 fF) due to the large geometric size which increases the noise and decreases the timing performance. [6]

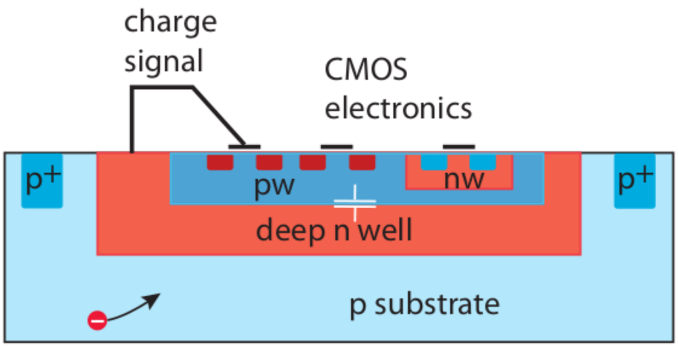

Figure 18: Scheme of large collection electrode DMAPS. [6]

Small collection electrode
In the small collection electrode design, a small n well is placed apart from the CMOS electronics as collection electrode (fig.19). This leads to a small collection node capacitance (5-20 fF) which favors the noise and timing performance. The longer drift times of the deposited charge due to the geometric layout is considered to have a negative impact on the radiation hardness. [6]

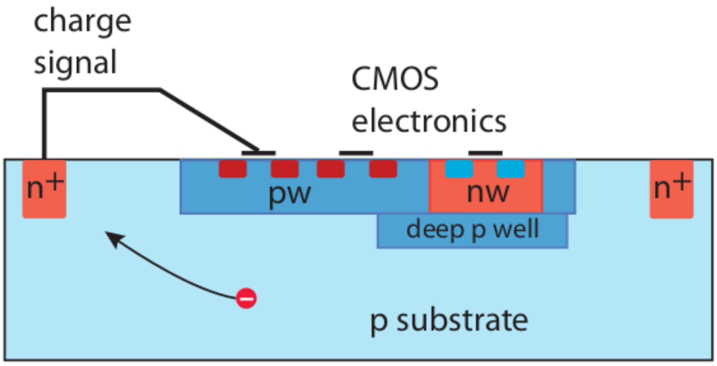

Figure 19: Scheme of the working principle of a small collection electrode DMAPS. [6]

A modified version of the small collection electrode design is shown in fig.20. An epitaxial layer is added together with a n-doped layer for strengthening the electric field laterally. This creates a potential minimum underneath the collection electrode, which is beneficial for the electron collection. [6]

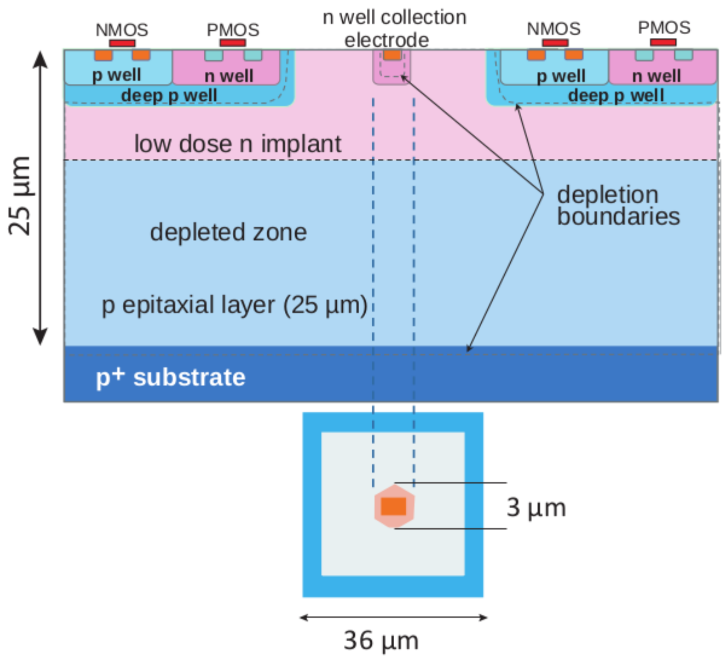

Figure 20: Modified design approach for small collection electrode DMAPS. [6]

3.2.1. RD50-MPW4

The RD50-MPW4 is a DMAPS with a large electrode design from the CERN-RD50 CMOS group. It is the fourth prototype following the HV-CMOS approach for radiation hardness fabricated with a 150 nm process from LFoundry. Two of in total four produced wafers were produced with backside processing. The RD50-MPW4 has a size of 5.63 mm x 6.30 mm and contains a pixel matrix of 64 x 64 pixel. Each pixel has a size of 62 µm x 62 µm. The readout of the pixel matrix by the digital periphery is realized with 32 FEI3 style double columns [18]. A block diagram is given in fig.21. [19]

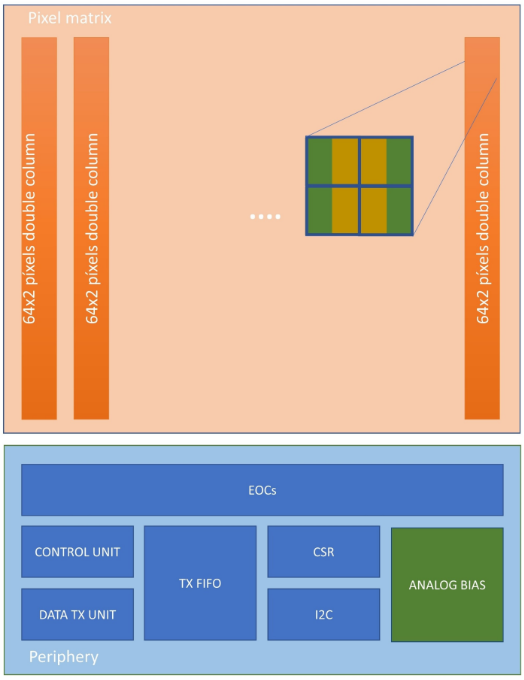

Figure 21: Block diagram of the RD50-MPW4. [19]

The chip has a global 8-bit time stamp based on a 40 MHz clock. A block diagram for the in-pixel electronics is given in fig.22. The in-pixel electronics consists of a bias circuit for the sensing diode, a pre-amplifier, a filter and a discriminator which defines a threshold. For the discriminator output, the time stamp leading edge (TS-LE) and the time stamp trailing edge (TS-TE) are stored in two 8-bit RAMs. Topside biasing is possible for all chips while backside biasing is only possible for the chips from the two wafers with backside processing. A bias block allows setting in total ten different bias voltages. They are depicted from the documentation in fig.1 together with their default settings. When setting the registers, they have to be converted into binary and inverted bit by bit. [19]

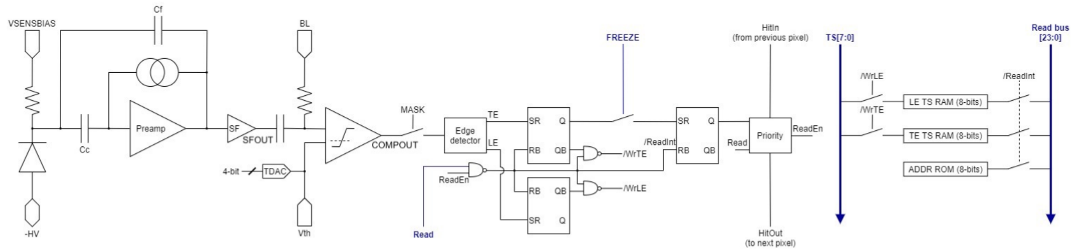

Figure 22: Block diagram of the in-pixel electronics of the RD50-MPW4. [19]

	Name	Nominal	Current	Voltage	Description
CH1	VPCOMP	44	10.1 μA	1.23 V	for comparator
CH2	VPTRIM	27	153 nA	1.24 V	for trim-DAC
CH3	VNSENSBIAS	13	2 nA	1.31 V	for DNWELL bias circuit
CH4	VBLR	25	6.6 nA	1.2 V	for high-pass filter
CH5	VNSF	18	1.03 μA	418.9 mV	for source follower
CH6	VNFB	45	400 nA	584.4 mV	for reset circuit
CH7	VPFB	25	6.6 nA	1.28 V	not used in this chip
CH8	VPBIAS, VNCASC	26	2.98 μA, 995 nA	1.02 V, 927 mV	for pre-amplifier
CH9	VN	42	6.02 μA	616 mV	for pre-amplifier
V_REF	VN_CS_BB	/	35 μA	540 mV	reference voltage

Table 1: Bias voltages and default settings of the RD50-MPW4. [19]

3.2.2. TJ-Monopix2

The TJ-Monopix2 is a DMAPS designed in 2020 in the small collection electrode approach with an epitaxial layer. It is the second iteration of this chip, which was originally designed to meet the requirements of the ATLAS Inner Tracking Detector. The TJ-Monopix2 is fabricated in the modified TowerJazz 180 nm process. It operates on a 160 MHz clock and has a time over threshold (ToT) resolution of 7 bits. The timestamping is done with a frequency of 40 MHz and the calculation of the ToT is done in a similar fashion as for the RD50-MPW4 using a TS-LE and a TS-TE. The matrix of the chip consists of 512 x 512 pixels with a size of 33.04 µm × 33.04 µm. The total size of the chip is 2 cm × 2 cm. The chip features two different front ends with in total four different pixel types with different electronic detection circuits called flavors (see fig.23). The four flavors are divided into two AC-coupled and two DC-coupled sections. An AC coupling to the front-end pre-amplifier input allows applying a positive high voltage bias at the collection electrode without saturating the frontend amplifier. [16, 20]

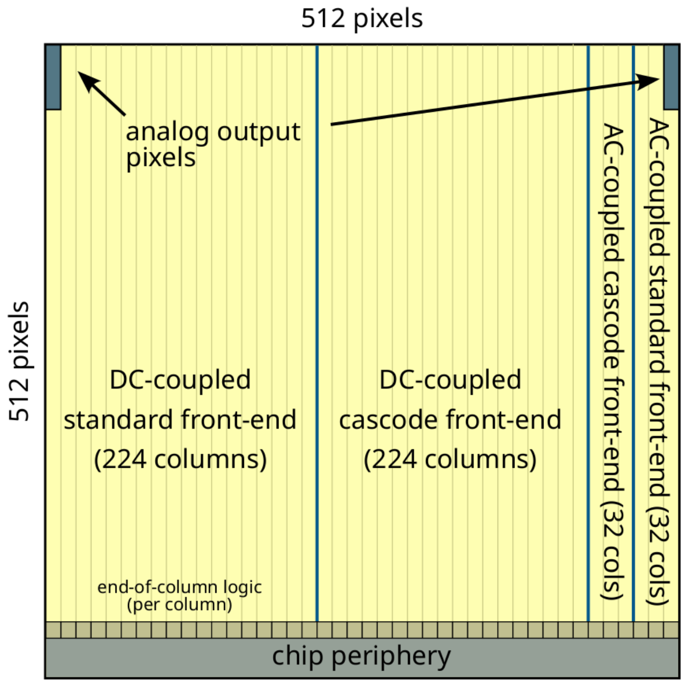

Figure 23: Design of the different front-ends of the TJ-Monopix2. [16]

The DC-coupled front end supports a bias voltage up to ≈ 10 V while the AC-coupled front end, also called high voltage front end, supports front side high voltage biasing up to ≈ 50 V. Both front ends feature two flavors which differ in the pre-amplifier design. The cascode flavors feature an extra cascode transistor which increases the pre-amplifier gain. The circuit of the analog amplifier is shown in fig.24. The achievable full depletion depth of the TJ-Monopix2 is limited by the thickness of the epitaxial layer, which is given as 30 µm by the foundry. Full depletion of unirradiated chips could be verified for the DC-coupled front end with a bias voltage of 6 V and for the AC-coupled front end for a bias voltage of 35 V. [16, 20]

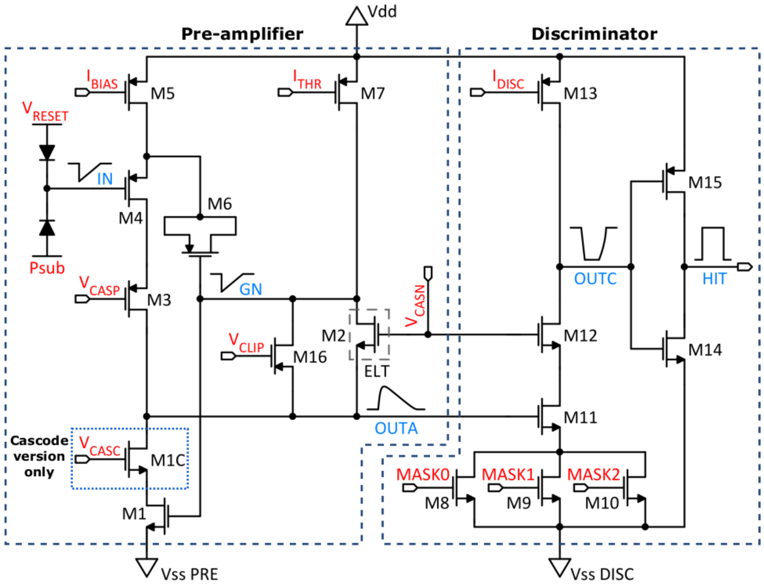

Figure 24: Schematic of the in-pixel analog amplifier circuit of the TJ-Monopix2 powered by V_{dd} (=VDDA). [20]

The TJ-Monopix2 is supplied via four different inputs listed in tab.2. The first amplifier stage shown in fig.24, which is powered by VDDA, is biased with the current IBIAS for noise reduction of the initial signal amplification. The 7-bit time stamp is distributed across the matrix with the bunch crossing ID (BCID) using Gray Code [21]. The BCID is powered by drivers from VDDP. The VPC sets the pre-charge current I_VPC, which sets the default charge for reading the pixel address.

Input	**Supply**
VDDA	analog part of the matrix
VDDD	digital part of the matrix
VDD_DAC	analog-periphery
VDDP	digital-periphery

Table 2: Power supply channels of the TJ-Monopix2.

3.3. Characterization of Detectors

3.3.1. Test beam

A particle detector can be tested and characterized in a so called test beam facility. These facilities provide a particle accelerator and a beam line where a particle beam can be extracted. In order to test a prototype chip, it is mounted as a device under test (DUT) in a beam telescope consisting of several layers of other detectors. The particle beam then gets directed through the telescope with the DUT mounted. The telescope is divided in an upstream part and a downstream part as illustrated in fig.25. Using the data from the telescope, single particle tracks can be reconstructed in an analysis framework (section 3.4) and the intersection of their trajectory can be compared with the actual data from the DUT. The obtainable observables are described in the next section.

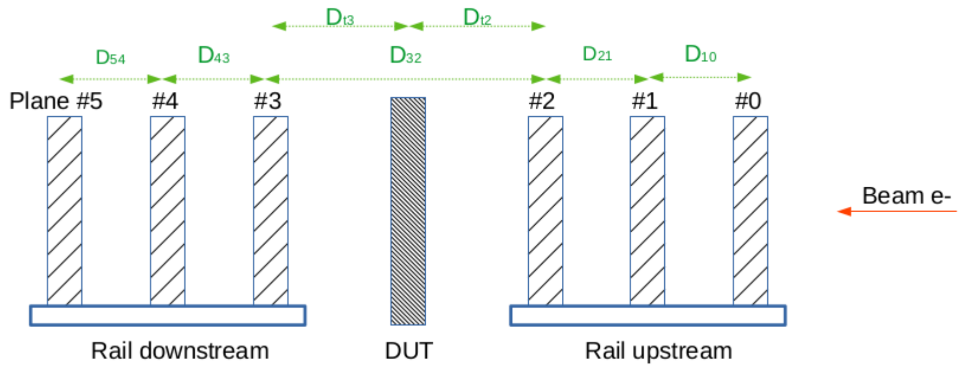

Figure 25: Scheme of a beam telescope consisting of 6 planes and a DUT. [22]

3.3.2. Observables

3.3.2.1. Time over Threshold

The ToT describes the time, in which the comparator output of a single pixel exceeds a given threshold. It is calculated by the difference between TS-TE and TS-LE. A plot illustrating this is given in fig.26.

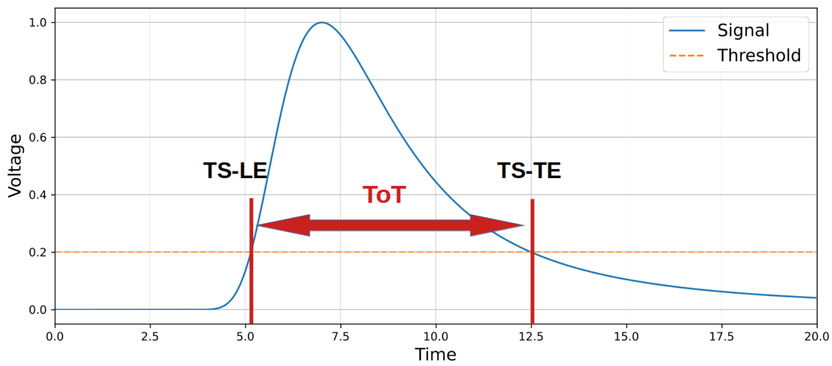

Figure 26: Scheme of the calculation of the ToT as the difference between the time stamps.

3.3.2.2. Correlations

Under ideal conditions (no scattering), the beam intersects all detectors orthogonally on a straight line. Because of that, the hits on the detector planes are correlated to each other. The correlation is obtained by calculating the difference of the hit position in one dimension of two detector planes. When defining a detector as reference plane, it is possible to determine a relative offset in the alignment. Due to interactions of the particles which cause scattering, several hits are needed for statistics. The obtained distribution of the relative difference in one dimension shows a pronounced peak as depicted in fig.27 which should be centered around zero for correct alignment.

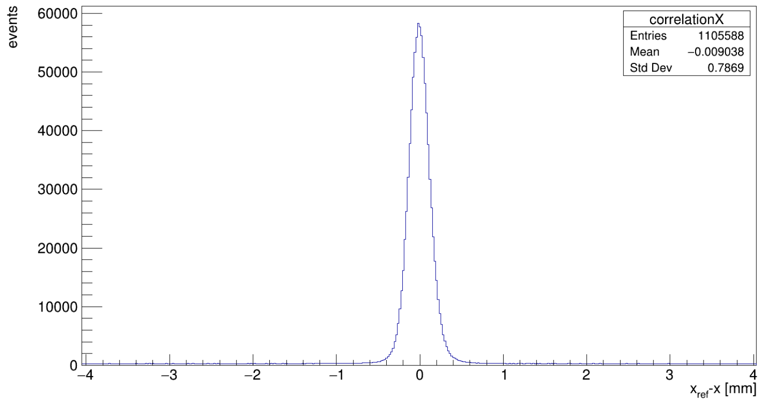

Figure 27: Correlation between two detector planes for correct alignment in x direction.

3.3.2.3. Cluster Size

A cluster defines a group of neighbored pixels which are active close in time. The reason for this is charge sharing between neighbored pixels. When a particle intersects a detector, it deposits charge in its volume. When the intersection is close to a boundary of two or more pixels as depicted in fig.28, it is possible that parts of the deposited charge are collected by several charge collection electrodes leading to more than one active pixel per particle intersection.

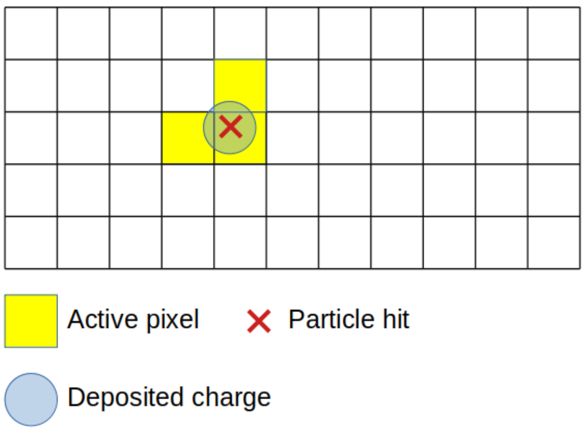

Figure 28: Illustration of the occurrence of clusters due to charge sharing.

3.3.2.4. Spatial Residuals

For calculating the spatial residuals, a prior track reconstruction with a beam telescope is mandatory. The spatial residuals x_{res} are defined by the difference between the reconstructed track intersection at the position of the DUT x_{track} and the actual associated hit position from the DUT data x_{hit} for one dimension as shown in eq.25 and illustrated in fig.29.

$$x_{res} = x_{track} - x_{hit} \tag{25}$$

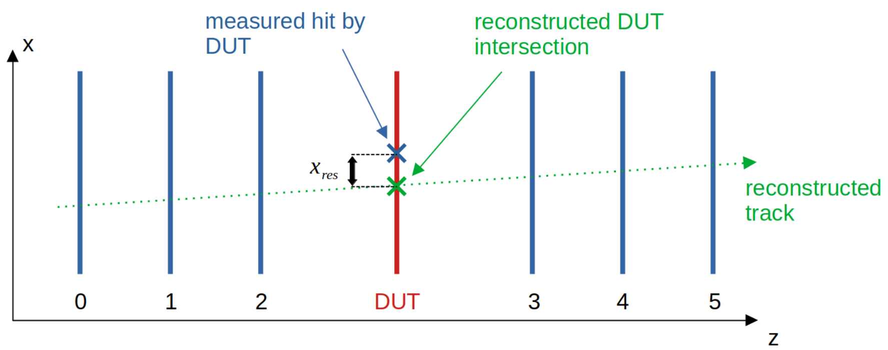

Figure 29: Illustration for the calculation of spatial residuals in one dimension for a single track.

3.3.2.5. Spatial Resolution

The spatial resolution x is calculated as the geometric mean of the standard deviation σ of the distribution of the residuals of the biased and unbiased residuals [23]. If the data from the DUT is included in the tracking procedure, the resulting residuals are called biased since the algorithm is forced to include the measured hit position on the DUT resulting in smaller residuals. For unbiased residuals, only the telescope data is used for the track reconstruction.

$$x = \sqrt{\sigma_{biased}\sigma_{unbiased}} \tag{26}$$

For measurements of the spatial resolution of pixel detectors with binary readout, the variance only depends on the pixel pitch p under the assumptions that the particle tracks are uniformly distributed, each track only fires a single channel and that the channel is only sensitive to a region $\pm\frac{p}{2}$ around its center (eq.27). With analog readout, the achievable spatial resolution can be improved by reconstructing the center of charge with the charge information from several channels. This procedure is called charge weighting. In order to improve charge sharing, a slight rotation of the detector with respect to the intersecting particles is possible. [24]

$$\sigma^2 = \frac{1}{p}\int_{-\frac{p}{2}}^{\frac{p}{2}} x^2 dx = \frac{p^2}{12} \tag{27}$$

3.3.2.6. Efficiency

The efficiency is the number of detected hits by the DUT associated to a reconstructed track n_{dut} divided by the number of intersecting tracks n_{track} as shown in eq.28.

$$\epsilon = \frac{n_{dut}}{n_{track}} \tag{28}$$

3.3.2.7. Timing

The timing resolution σ_t of a detector is given by the standard deviation of the distribution of the time residuals t_{res} which is the difference between the reconstructed track intersection t_{track} with the DUT data t_{DUT}.

$$t_{res} = t_{track} - t_{DUT} \tag{29}$$

3.4. Analysis Framework

A well established analysis framework for the analysis of test beam data is Corryvreckan [25]. Its task is to interpret data, reconstruct tracks and thereby produce the above mentioned observables. Corryvreckan needs a *geometry file* which defines the geometry and the used detector types and a *config file* which defines the different modules and their parameters as input. Examples which have been used in this thesis can be found in the appendix A.2.

3.4.1. Event Building

Corryvreckan consists of a collection of modules and an event loop which processes data from all detectors given in the geometry file sequentially for each *event* defined on the *clipboard*. An event is a Corryvreckan object which stores meta-information about the data currently processed. Event loader modules read external data sources and convert them to Corryvreckan objects placed on the clipboard. The first event loader defines events with time windows. Additionally, a trigger ID can be used. Following event loaders can only access the defined events and compare their time or trigger ID of currently processed data with them. If triggered devices without time stamps are used in combination with un-triggered devices, a trigger logic unit (TLU) is required. A TLU is an external device which relates time stamps and trigger IDs. If the event definition is done by the TLU, a matching time window can be adjusted with the parameter *adjust_event_times* from the module *EventLoaderEUDAQ2*. [25]

3.4.2. Modules

Below, an overview of different module types with available examples which are needed for the analysis is given. They have to be executed after the event building.

3.4.2.1. Clustering

In this step, pixels which are active close in space and time and therefore likely result from a single particle are grouped into clusters. Clustering is needed before track reconstruction. Available modules for Corryvreckan are *ClusteringSpatial* and *Clustering4D*.

3.4.2.2. Tracking

This module reconstructs tracks by fitting clusters on different detectors which are likely to result from a single particle to common tracks. The reconstruction can either follow a *straight line fit* which is suitable for high energies where scattering can be neglected or a general broken line (GBL) fit. The GBL fit assumes a straight line between two adjacent planes and allows for an angle dependent on the energy and material budget at each layer which acts as a free parameter for the fitting algorithm (see fig.30). For lower energies, this fit should be used. Further parameters of the tracking module are the number of *minimal hits on track* which defines how many layers must have a cluster assigned to a reconstructed track in order to use it and the *momentum* which defines the beam energy. For the tracking procedure, the DUT should in general be excluded to avoid introducing a statistical bias on the observables depending on the tracks. Tracking can be done with the module *Tracking4D*.

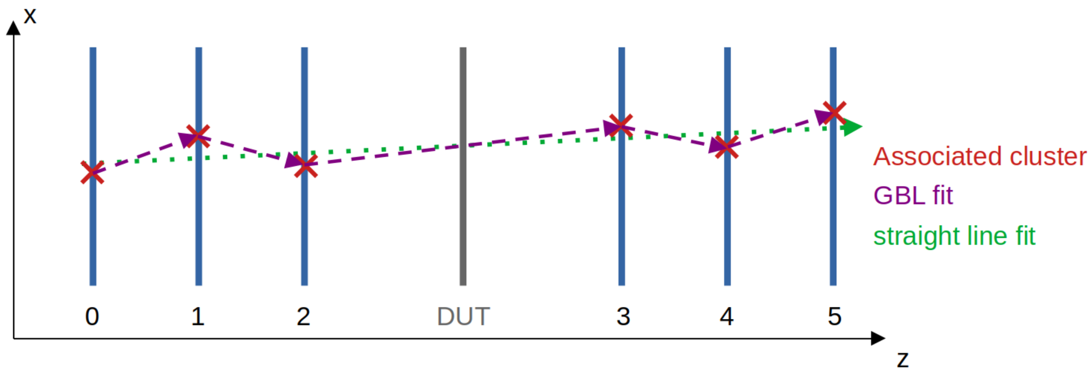

Figure 30: Scheme of straight line fit and GBL fit for single particle tracking.

3.4.2.3. DUTAssociation

This module is applied after tracking. It assigns clusters on the DUT to reconstructed track intersections. The parameter *spatial cut relative* defines the maximum distance between a cluster and the position of the track intersect in order to count as a hit in multiples of the resolution specified relative to the intrinsic resolution of the DUT.

3.4.2.4. Analysis

Further important modules are *AnalysisEfficiency*, *AnalysisDUT* and *Analysis-Timing* which are needed to evaluate different observables. A list of all available modules together with a description can be found in [25]. Another feature which can be used for the analysis is masking. If one or more pixels are masked, they are ignored in the analysis. So if a track intersects in the region of a masked pixel of the DUT, it will not reduce its efficiency. Masking can be used to exclude noisy pixels or disabled areas of a chip from the analysis.

3.4.3. Alignment

Before observables can be extracted from test beam data, an alignment of the detector planes has to be done which consists of several steps. The initial position of each detector has to be measured manually and entered to Corryvreckan in the geometry file. By defining only the positions along the beam axis with an accuracy in the order of mm, a pre-alignment must be done using the correlations of the detectors. Since this method is not accurate enough and does not take rotations of the detectors into account, a fine alignment has to be performed afterwards by fitting the detector positions to the track intersection points. An algorithm, depending on the chosen alignment module, finds the optimum of the displacement of the detectors with respect to a chosen reference plane and modifies the geometry file. It is recommended to first align the telescope and then align the DUT separately with an already aligned telescope geometry. [25]

4. Performance studies RD50-MPW4

This thesis contains the results of three different test beams conducted at the Deutsches Elektronen-Synchrotron (DESY) (see sec.4.1.1) and MedAustron (see sec.4.1.2) with the RD50-MPW4. At DESY, four unirradiated samples with and without backside processing were measured from 22.04.2024 to 29.04.2024. The aim of the first test beam with this chip was to characterize its performance and study differences due to backside processing. At the second test beam at DESY from 30.09.2024 to 7.10.2024, four irradiated samples in combination with an unirradiated for reference were measured in order to see the impact of different fluences on the performance of the chip. The test beam at MedAustron took place on 28.08.2024 to verify the functionality of the setup before the second DESY test beam.
All measured samples are summarized in tab.3. The naming corresponds to the wafer they are taken from, followed either by their fluence or a capital letter for the institute they belong to.

Chip	**Backside Processing**	**Fluence [$n_{eq}cm^{-2}$]**	**Institute**
W3-N	yes	0	NIKHEF
W3-V	yes	0	HEPHY
W8-V	no	0	HEPHY
W8-L	no	0	University of Liverpool
W3-1E14	yes	1E14	HEPHY
W3-3E14	yes	3E14	University of Liverpool
W8-1E15	no	1E15	HEPHY
W3-1E16	yes	1E16	HEPHY

Table 3: Overview of all measured samples.

4.1. Experimental Setup

The experimental setup consists in general of a beam line, a telescope and the DUT with a corresponding data acquisition systems (DAQ) as shown in the scheme depicted in fig.25. For the RD50-MPW4, the Cribou DAQ [26] was used. The communication and data storage between the different components during data taking was done by the data acquisition software framework EUDAQ2 [27]. To synchronize the individual DAQ systems, an AIDA-2020 TLU [28] was used for all test beams. The data used in this thesis were collected at test beams at the medical facility MedAustron and the test beam facility at DESY.

4.1.1. DESY

The DESY test beam facility is located at its campus at Hamburg-Bahrenfeld. It provides three independent beam lines. The particles are extracted from the DESY II synchotron. The beam lines feature electrons and positrons with momenta between 1 and 6 GeV/c [29]. For the test beams in this thesis, electron beams with a momentum of about 4.2 GeV/c and a particle rate of about 10 kHz were used. As telescope, 6 ADENIUM planes [22] provided from the test beam facility were used. The telescope provides a pointing resolution better than 3 µm. To achieve appropriate timing resolution, an additional layer containing a TelePix [30] was added to the telescope planes. It provides track time stamping with a precision of about 5 ns and allows to define a region of interest for the telescope readout. The region of interest is beneficial for the data taking and analysis. Due to the bigger size of the telescope detectors compared to the DUT, many recorded tracks do not intersect its position. By triggering on a region of interest, these tracks are ignored in the data taking process.

4.1.2. MedAustron

MedAustron is a particle therapy center located in Wiener Neustadt in Austria containing a synchrotron. It features a beam line for clinical and non clinical research with proton and helium beams with energies up to 800 MeV and rates up to 10×10^9 Hz [31].

The beam telescope at MedAustron consists of four DSSDs with a thickness of 300 µm, an active area of $25 \times 50\,\text{mm}^2$ and two plastic scintillators [32].

4.2. Efficiency and Performance Measurements without radiation damage

4.2.1. Trade off between Efficiency and Resolution

In the analysis, the efficiency and the spatial resolution can change depending on the used parameters. The parameter *spatial_cut_rel* in the *DUT association module* defines the maximum distance between a reconstructed track intersection and a cluster on the DUT in multiples of the resolution of the detector given in the geometry file. If the cut is chosen too narrow, the spatial resolution improves at cost of the efficiency due to rejected tracks. This trade off is illustrated in fig.31. The spatial resolution x is normalized to the lowest value x_{min} (best resolution) which defines 100 % as shown in eq.30. A saturation of the efficiency as well as for the spatial resolution is found at a value of five. This value was used for the analysis in this thesis.

$$x_{norm} = 100 \cdot (2 - \frac{x}{x_{min}}) \tag{30}$$

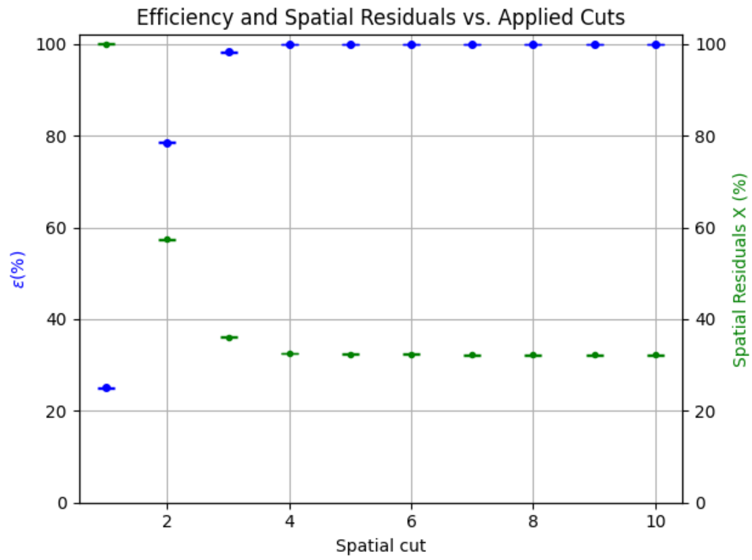

Figure 31: Trade off between the spatial resolution normalized to the minimum value and efficiency depending on the applied relative cut for a given detector resolution of 17.898 µm in the geometry file.

4.2.2. Standard Settings

From prior test beams and lab measurements, the full depletion of the detector was expected to be at a bias voltage of around 190 V [33]. Because of that, measurements with a duration in the order of one hour, referred to as statistic runs, were taken for all chips at a threshold of 40 mV. The mean values for ToT and cluster size as well as efficiency are shown in tab.4. The deviation of the mean values refers to the standard error of each data set. In fig.32, an example distribution for the ToT and cluster size is shown. W8-V is given with a lower threshold of 20 mV since no suitable run was taken for this sample with a bias voltage of 190 V. The chips show some sample variation but no obvious difference of the backside processed chips is visible. All detectors work with an almost perfect efficiency.

Chip	Threshold [mV]	ToT [LSB]	Cluster Size	Efficiency [%]
W8-V	20	6.870 ± 0.006	1.322 ± 0.001	99.99
W8-L	40	8.076 ± 0.005	1.349 ± 0.001	99.89
W3-V	40	8.529 ± 0.005	1.368 ± 0.001	99.99
W3-N	40	7.969 ± 0.005	1.321 ± 0.001	99.99

Table 4: Results of mean values for ToT and cluster size for standard settings (190V bias voltage) of unirradiated chips at room temperature.

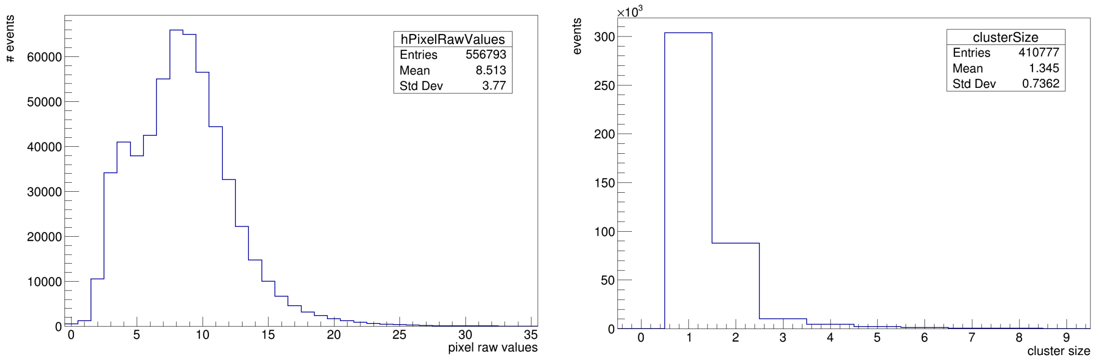

(a) ToT distribution

(b) Cluster size distribution

Figure 32: Distributions for a) ToT and b) cluster size for W3-V.

4.2.3. Impact of Bias Voltage and Threshold

In order to evaluate the impact of bias voltage and threshold on the chip performance, bias and threshold were scanned. All data in this section were taken at the first DESY test beam in April 2024. Due to restricted measurement time and different behavior of the chips, not all samples could be measured in the same ranges and granularity. The minimum and maximum values for the measured bias voltage and threshold are given in tab.5 together with the applied threshold for the bias voltage scans. The threshold scans were all done with a bias voltage of 190 V. In the analysis, masking was applied for all chips because of disabled pixels due to noisy behavior.

Chip	Range Bias Voltage [V]	Fixed Threshold [mV]	Range Threshold [mV]
W8-V	25-190	20	20-395
W8-L	35-500	30	20-395
W3-V	2-450	40	35-395
W3-N	2-500	40	20-380

Table 5: Minimum and maximum values for the measured bias voltage and threshold for unirradiated samples.

4.2.3.1. ToT

The ToT increases considerably for all samples until a bias voltage of about 190 V is reached as fig.33 shows. This behavior suggests that the full depletion voltage of the samples is around 190 V since higher bias voltage does not lead to an increase of the sensitive detection volume in the sensors from this voltage on. After the 190 V bias voltage, the samples show only a minor increase of the ToT with further increasing bias voltage. W8-V has the lowest maximum value with about 6.9 LSB at 190 V. The maximum measured ToT value was reached by W3-V with a ToT of 8.7 LSB at a bias voltage of 450 V.

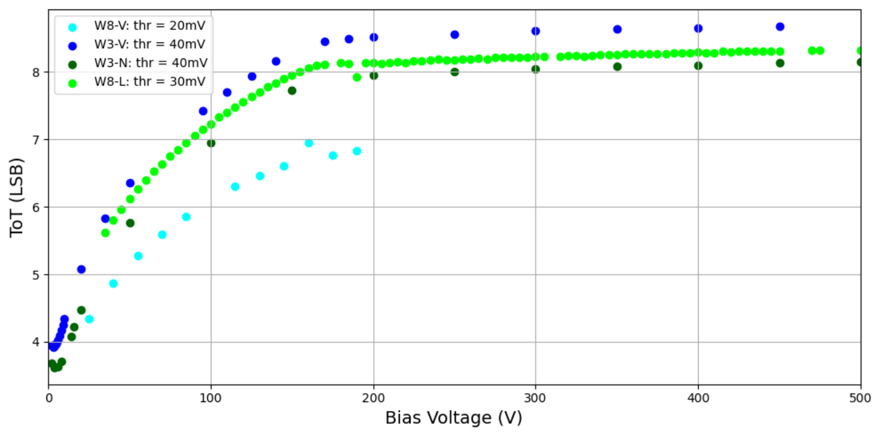

Figure 33: Time over threshold versus bias voltage for four unirradiated samples.

4.2.3.2. Cluster Size

The cluster size for perpendicular tracks in fig.34 shows a maximum of about 1.38 pixels per cluster around 190 V. This is a further indicator that the unirradiated samples are fully depleted at this bias voltage. Further increase of the bias voltage results in a smaller cluster size due to the suppression of the diffusion current from the higher electric field in the sensor.

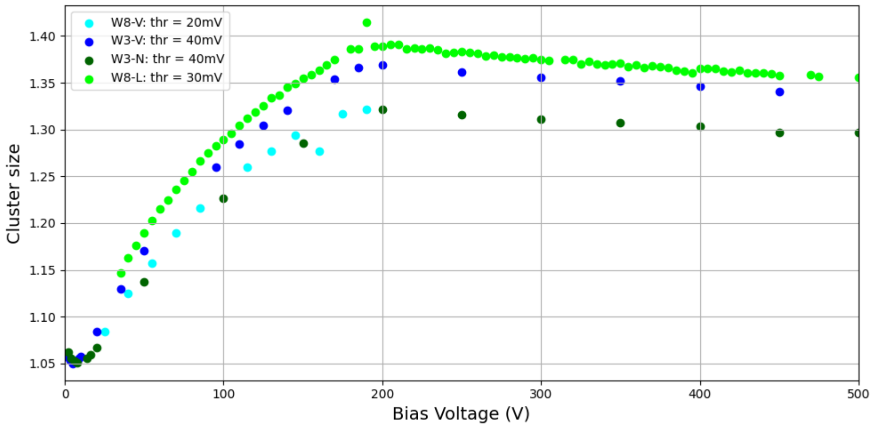

Figure 34: Cluster size versus bias voltage for four unirradiated samples.

4.2.3.3. Efficiency as a function of Threshold

The maximal applicable threshold of a sensor before loosing signal due to not detected hits is of interest especially for samples with radiation damage, because they suffer from higher dark current and noise compared to samples without radiation damage. In order to find a threshold range at which the RD50-MPW4 can be operated without signal loss, a scan of this parameter was done with the four samples without radiation damage. The efficiency over the applied threshold is shown in fig.35 together with a charge calibration. The charge calibration was done in laboratory measurements using injections and the in-pixel injection capacitance as described in [33]. W8-V is the first sample which has an efficiency lower than 99 % at a threshold of 185 mV. The next ones are W8-L and W3-N at 260 mV and W3-V at 290 mV. Due to the lack of statistic and the high sample variation, no evident difference between the backside processed and the normal samples can be stated.

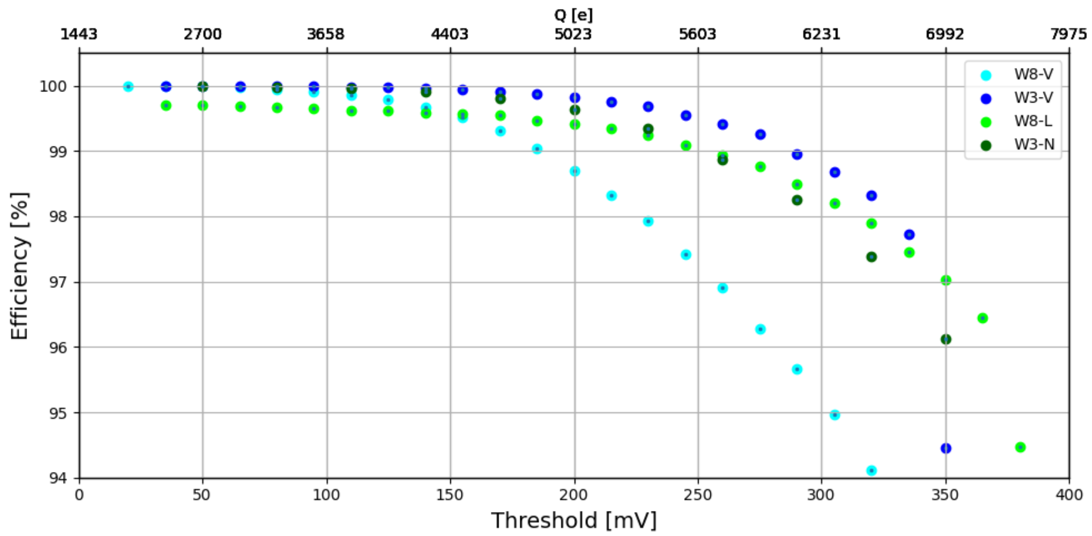

Figure 35: Efficiency versus threshold for four unirradiated samples.

4.2.4. Spatial Resolution

The spatial resolution was calculated as the geometric mean (eq.26) of the standard deviation of the truncated root mean square (rms) of the biased and unbiased spatial residuals. The relation for the standard deviation of the rms of a data set with N samples is given in eq.31. Truncated rms refers to the drop of a fixed percentile of the data for the calculation of the rms as illustrated in fig.36. For a truncated rms to the innermost 99 % of the distribution, which was used in this thesis, the 0.5 % of all entries to the left of the red line (lower values) and the 0.5 % of all entries to the right of the green line (higher values) of each residual distribution were cut. This procedure minimizes the impact of outliers and ensures a reproducible data evaluation.The binary resolution of the RD50-MPW4 with a pixel pitch of 62 µm evaluates with eq.27 to approximately 17.90 µm.

$$x_{rms} = \sqrt{\frac{\sum_i (x_i - \langle x \rangle)^2}{N}} \tag{31}$$

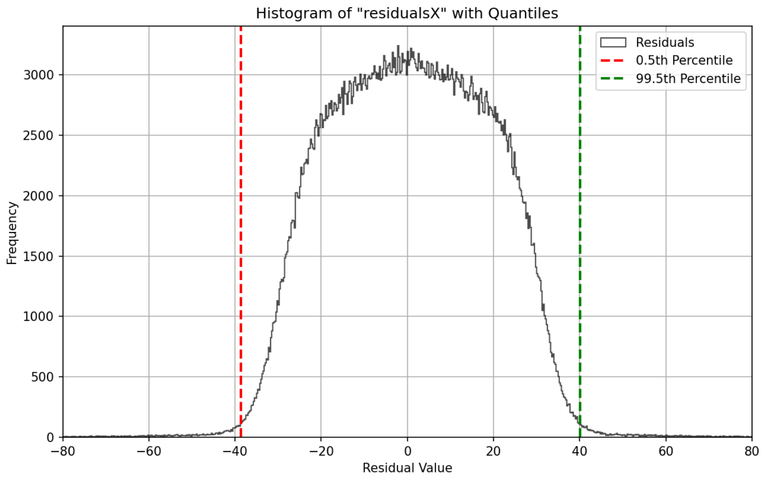

Figure 36: Evaluation of truncated root mean square for spatial residuals.

The evaluation of the spatial resolution in X and Y direction is shown in tab.6 for all four samples operated with standard settings (see sec.4.2.2). W8-V performs the best with a resolution of 15.98 µm in X direction which is below the binary resolution due to charge weighting. The resolution in Y direction performs slightly worse for all samples. A possible reason for this behavior is the slightly higher cluster width in X direction which is beneficial for charge weighting.

Chip	σ_x [µm]	**Cluster Width X**	σ_y [µm]	**Cluster Width Y**
W8-V	15.98	1.169 ± 0.0008	16.05	1.167 ± 0.0008
W8-L	18.26	1.181 ± 0.0008	18.89	1.179 ± 0.0008
W3-V	16.27	1.191 ± 0.0009	16.32	1.188 ± 0.0009
W3-N	16.28	1.167 ± 0.0007	16.32	1.166 ± 0.0007

Table 6: Results of the spatial resolution with truncated rms (99 %) for unirradiated chips operated with standard settings.

4.2.5. Timing

The 8-bit timestamp of the RD50-MPW4 covers 256 values which corresponds with a 40 MHz clock to a time of 6400 ns. If an overflow occurs a signal is sent to the DAQ system which counts the number of overflows. The readout of a stored hit signal in the matrix can take a few clock cycles, which can cause a mismatch with the overflow counter which is assigned to the hit after the readout. A mismatch of one leads to a time difference of -6400 ns. For the distribution of the time residuals, this leads to a main peak centered around zero and an overflow peak with a distance of 6400 ns (see fig.37). At the test beam in April 2024, the register *CONF_REG_TS_CTRL* of the chip was configured wrongly (0x00 instead of 0x04) and thus the external signal to reset the timestamp counter was disabled. This external signal is toggled by the DAQ at every start of a new run, to ensure that the timestamp counter starts counting from 0. As a result of the wrong setting, the reset did not happen and the main peak was shifted randomly in the region of -6400 ns to 0 ns. In order to extract timing information from this distribution, a manual time shift moving the main peak to zero ns and a time cut of 800 ns were applied in the analysis. The time cut removes the overflow peak from the data which allows calculating the standard deviation of the main peak at the cost of an efficiency drop of about 20 %.

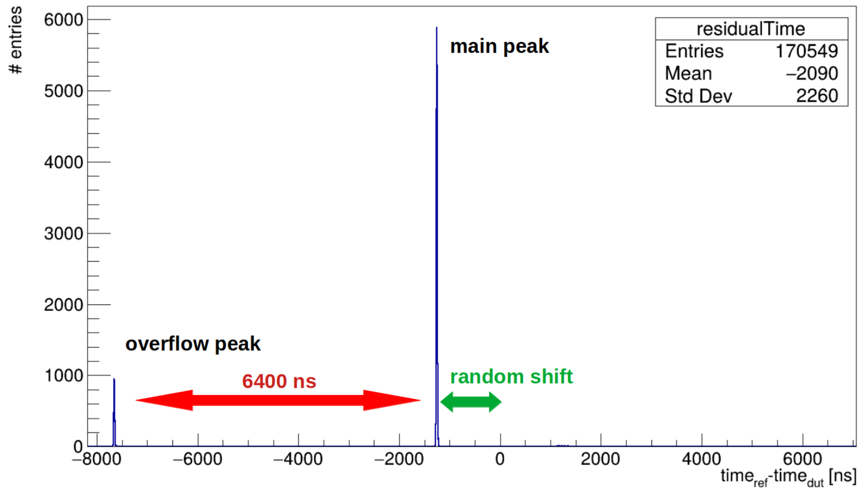

(a) Uncorrected time residuals with a random shift of the main peak and an overflow peak in a distance of 6400 ns.

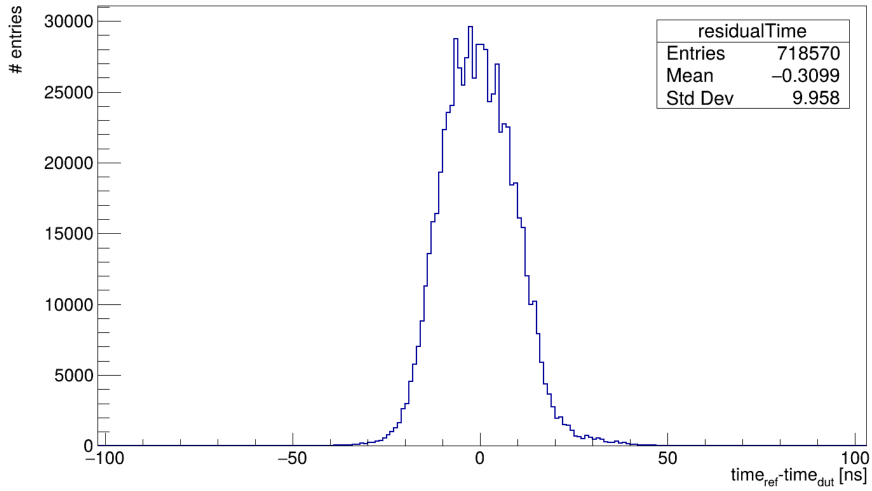

(b) Time residuals after correction of the offset and applied time cut.

Figure 37: Time residuals of the RD50-MPW4 of the sample W8-V.

The timing resolution is evaluated as described above from the main peak by means of a rms truncated to the innermost 99 % of the distribution. The results for unirradiated samples are shown for the threshold scans in fig.38. At a threshold of 40 mV, the time resolution is about 9 ns and increases with increasing threshold linearly up to 10 ns at 320 mV. Above this value, no reasonable timing information can be measured since the electronics is not designed for such high voltages for the threshold.

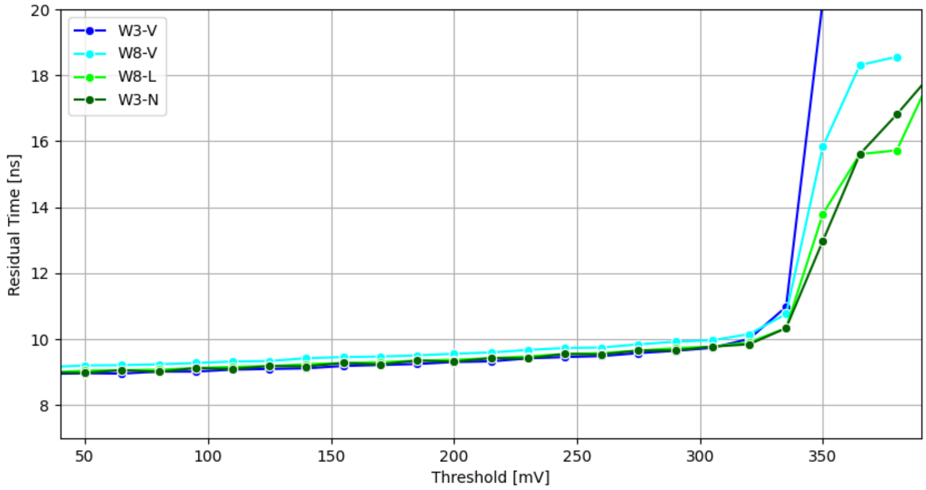

Figure 38: Residual times versus threshold for unirradiated samples.

4.2.6. Impact of DAC Settings

The digital-to-analog converter (DAC) settings defined in the bias block (see tab.1) influence the performance of the chip. Lab measurements showed that the reset current (VNFB) influences the threshold and the ToT. The data used in this section was collected at a test beam at MedAustron in August 2024. The measurements were done with the sample W8-V with the chip being operated at a threshold of 250 mV and a bias voltage of 190 V. The values of the DAC settings refer to the programmed, bitwise inverted values. Because of that, the default value of 45 of the VNFB corresponds to a value of 18. The reset current is applied in the preamplifier electronics. The gathered charge of the collection electrode from deposited charge of a traversing charged particle is further processed with the preamplifier which works as integrator amplifier circuit. The reset current is used for the reset of the integrator circuit. The higher the DAC setting of the VNFB is set, the longer it takes the reset current to reset the integrator circuit.

In fig.39, an increase of the mean values of the cluster size and the ToT can be observed with increasing VNFB. With a VNFB of 60, the cluster size increases from 1.09 (nominal setting) to 1.21 and the ToT increases from 6.55 LSB (nominal setting) to 59.73 LSB. In fig.40, the corresponding ToT distributions are shown for selected VNFB values.

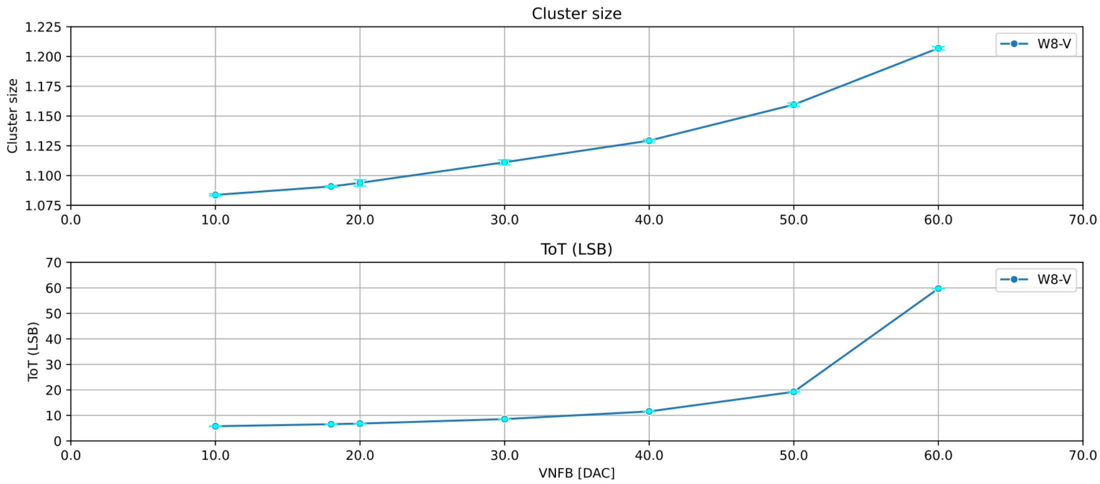

Figure 39: Increase of cluster size and ToT with increasing VNFB in DAC units.

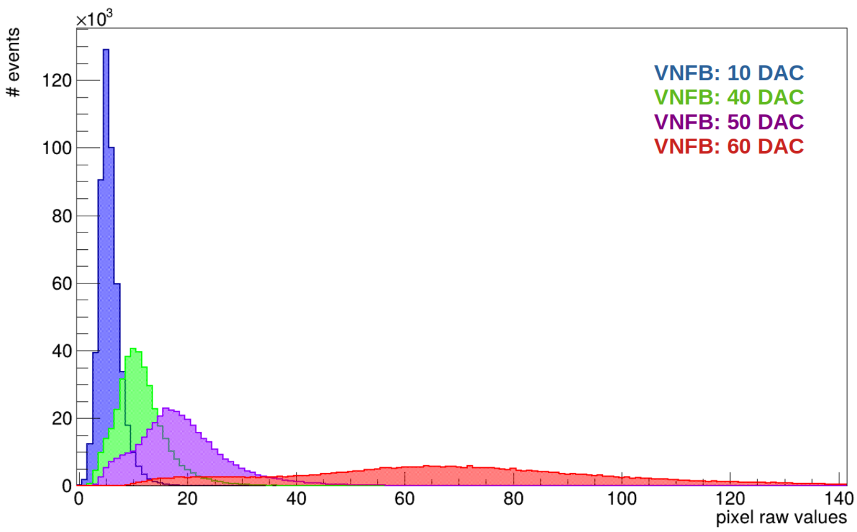

Figure 40: ToT distributions for selected VNFB settings.

Due to the high threshold of 250 mV, the chip did not show an efficiency of 99.99 % as in the previous test beam. By increasing the VNFB, the effective threshold slightly reduces, resulting in higher efficiency as shown in fig.41. In the measurements, the efficiency could be increased from 97.2 % (nominal setting) to 98.5 %.

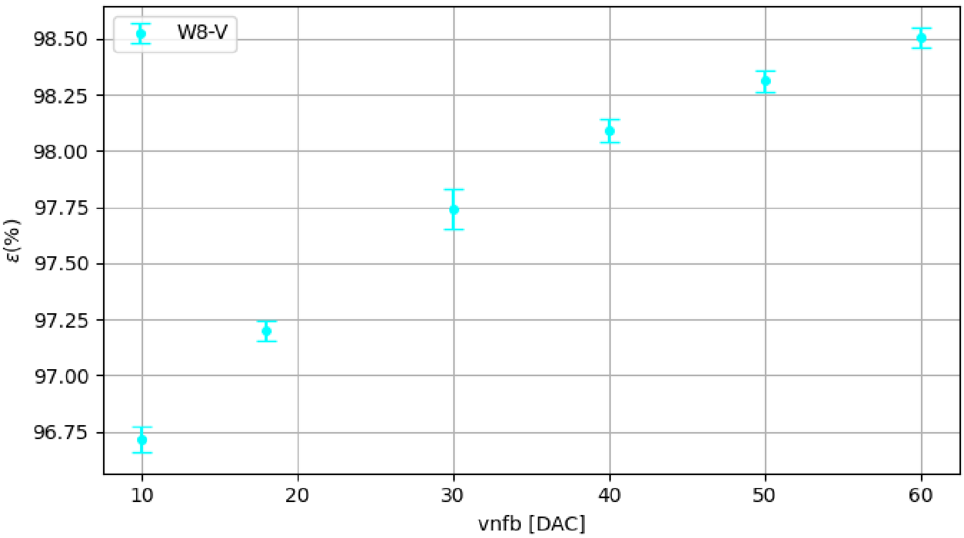

Figure 41: Efficiency versus VNFB for W8-V.

With increasing VNFB, the amount of mismatched entries with the overflow counter increases. At a VNFB of 60, all entries have a mismatch of one because the recharge current takes too long to reset the capacitor at the preamplifier circuit. This is indicated by an offset of $-6400\,\mathrm{ns}$ of the time residuals. A direct comparison for the time residuals with a VNFB of 50 and 60 is given in fig.42.

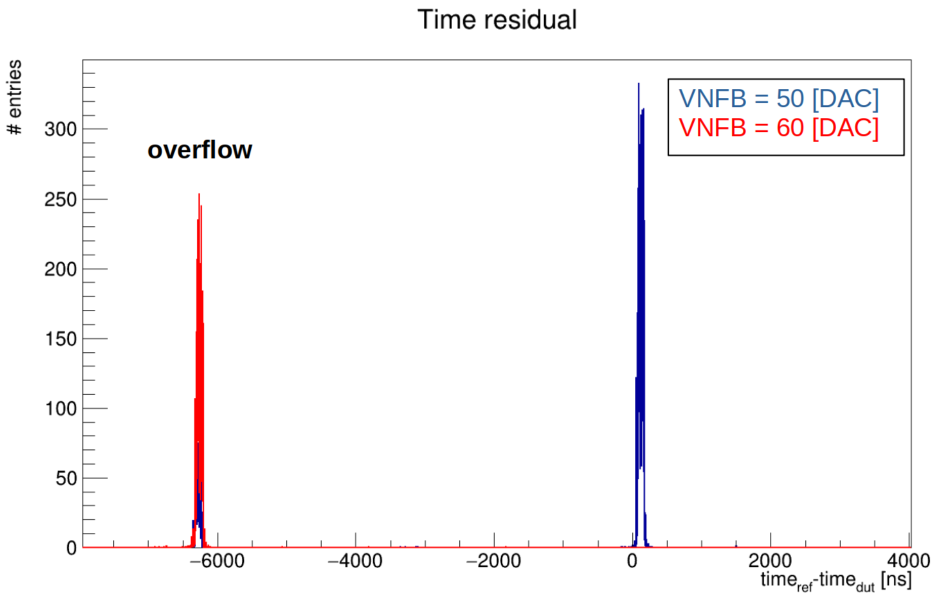

Figure 42: Comparison of time residuals of a measurement with a VNFB of 50 (blue) and 60 (red) of W8-V.

4.3. Characterization of irradiated samples

Four differently irradiated samples were measured to test the radiation hardness of the RD50-MPW4. The samples were irradiated with neutrons at the TRIGA Mark III reactor in Ljubljana. The data used in this chapter was collected during a test beam at DESY in October 2024. The irradiated samples with backside processing (W3-1E14 and W3-3E14) were measured with backside and topside biasing choosable via a jumper on the printed circuit board (PCB). The measurements from W8-1E15 suffer from a lack of statistics because it broke down during the test beam due to being operated at a too high bias voltage of 580 V. The sample which was irradiated with a fluence of $1 \times 10^{16}\, \mathrm{n_{eq}cm^{-2}}$ could still respond to I^2C messages but was not capable of collecting data to be analyzed. However, correlations could still be extracted from the data.

4.3.1. Cooling Setup

Due to the increased leakage current of irradiated sensors, a cooling setup was needed (see fig.43). The DUT was mounted inside a 3D printed box. The PCB of sample in the box was cooled via a copper block connected to a Peltier cooler. For good thermal conduction, a thermal conductive pad was placed between the copper and the DUT. The temperature was measured at the cold and hot side of the Peltier element, the copper block and the PCB of the DUT. The setup allowed to cool down the copper to approximately -15 °C.

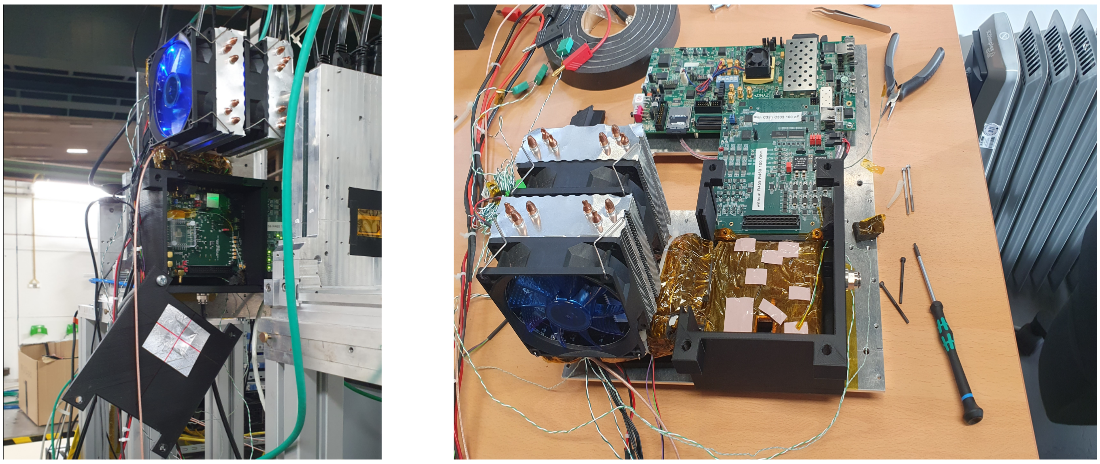

(a) (b)

Figure 43: Cooling setup for the RD50-MPW4 a) mounted in the beam telescope b) without DUT.

4.3.2. Observed Impact of Radiation Damage

For the samples W3-3E14 and W8-1E15, malfunctions most likely resulting from the irradiation process could be observed (see fig.44). Since the samples were not tested in a test beam setup before the irradiation process, it cannot be assured that some defects result from the production. For W3-3E14, the double column 44/45 showed a less efficient behavior than the rest of the matrix and for W3-1E15 the double column 32/33 was not working at all. Furthermore, the overflow counter was not usable for this sample. For the sample W3-1E14, no damage was observed. In the analysis, only the broken down double column of W3-1E15 was masked.

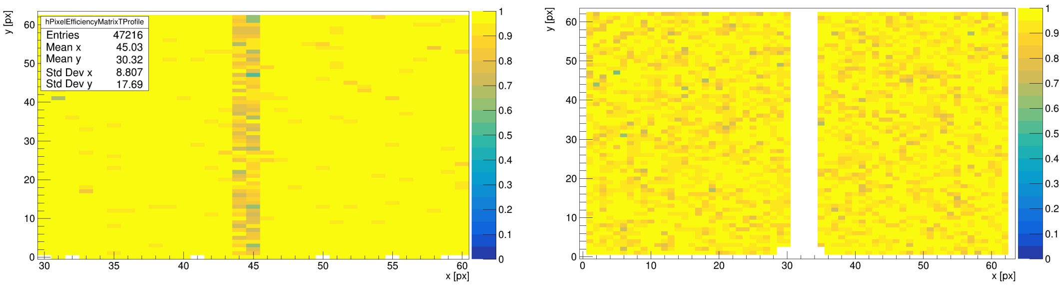

(a) W3-3E14 (b) W8-1E15

Figure 44: Efficiency maps for a) W3-3E14 and b)W8-1E15.

4.3.3. Bias Voltage Scans

The impact of the bias voltage on the performance of irradiated RD50-MPW4 samples was studied by applying increasing values in 10 V steps. The threshold settings and ranges of the bias voltage scans are given in tab.7. The chips were operated with the lowest possible threshold before running into noise problems. For W8-V, no higher bias voltage than 280 V was applicable. This sample was mainly used to verify the correct working of the setup. As reference for unirradiated samples, the results from W3-V from sec.4.2 will be used since it was produced from the same wafer as most of the irradiated chips.

	W8-V	W3-1E14	W3-1E14	W3-3E14	W3-3E14	W8-1E15
Biasing	topside	backside	topside	backside	topside	topside
Thr [mV]	100	200	200	50	50	70
Range [V]	10-280	20-500	10-500	10-500	10-500	190-560

Table 7: Threshold settings and scan ranges for bias voltage scans with irradiated samples.

4.3.3.1. Efficiency

Up to a fluence of $3 \times 10^{14}\,\mathrm{n_{eq}cm^{-2}}$, all samples could be operated at an efficiency of 99 % as shown in fig.45. For the sample W8-1E15, an efficiency of 98 % at a bias voltage of 560 V could be measured before it broke down. Better efficiency is likely to be achievable for this fluence with further tuning of the DAC settings. At a fluence of $10^{15}\,\mathrm{n_{eq}cm^{-2}}$, the RD50-MPW4 could still be operated but no useful data could be gathered.

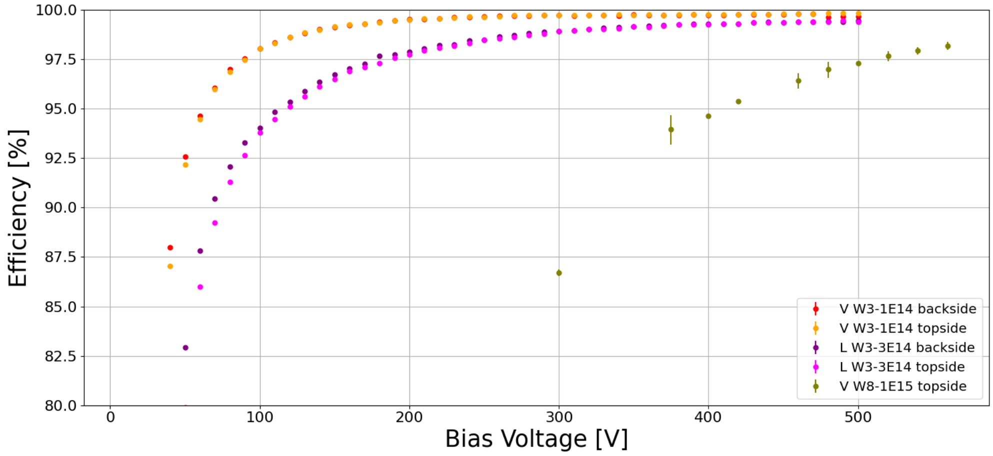

Figure 45: Efficiencies of the bias voltage scans with the irradiated samples.

4.3.3.2. ToT

For the irradiated samples, the maximum ToT decreases (16 LSB for 1E14/ 8 LSB for 3E14) with higher fluences as depicted in fig.46. However, the unirradiated reference sample only reaches a maximum ToT of 7.07 LSB. The reason for this is unclear. The sample W3-1E15 performs equally with backside and topside biasing.

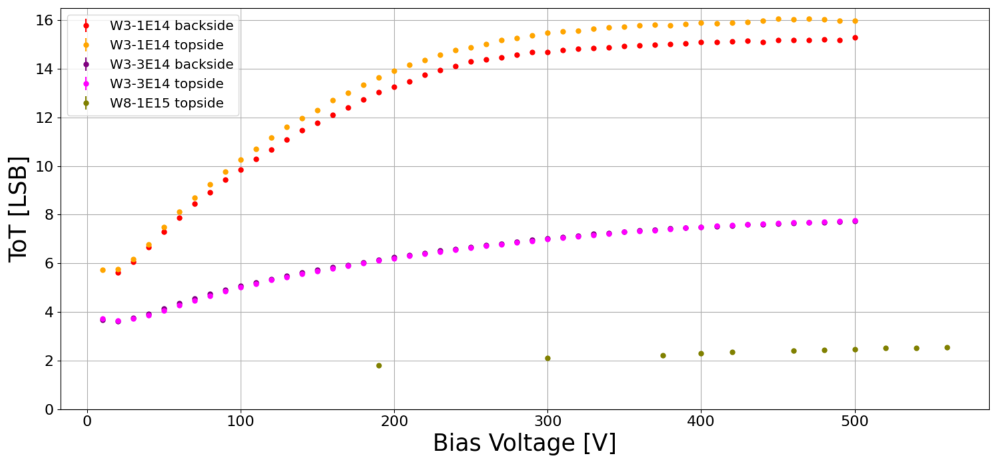

Figure 46: ToT values of the bias voltage scans of irradiated samples.

4.3.3.3. Cluster Size

The cluster size of W3-1E14 saturates at about 300 V bias voltage which indicates the full depletion of the sensor. Topside or backside biasing does not show an effect on this behavior. For W3-3E14, a complete saturation cannot be observed in the measured range, but it can be assumed to be around 500 V. For a fluence of $10^{15}\,n_{eq}cm^{-2}$, no saturation of the cluster size was observed under 560 V as shown in fig.47.

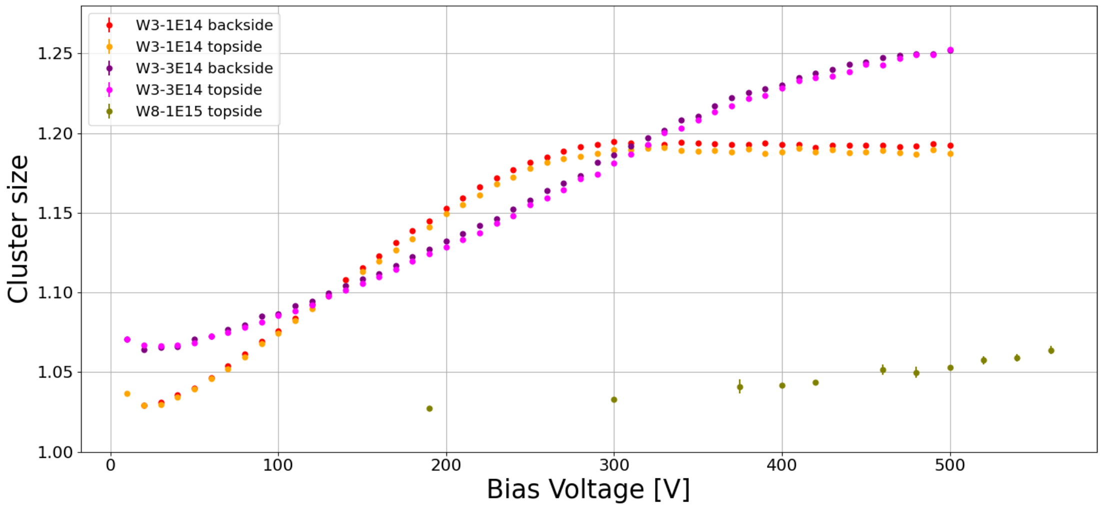

Figure 47: Cluster sizes of the bias voltage scans of irradiated samples.

4.3.3.4. Spatial Resolution

The spatial resolution increases from a global minimum at low bias voltages to a maximum and decreases again until it reaches a local minimum around the full depletion voltage as shown in fig.48. The good spatial resolution for under depleted sensors results from corner effects shown in the in-pixel efficiency maps in fig.49. The low efficiency in the corners of the pixels leads to the exclusion of tracks which are further away from the center of the pixels resulting in better spatial resolution at the cost of efficiency. Due to charge weighting, the bigger cluster sizes of the samples with higher fluences lead to an improvement of the spatial resolution. The spatial resolution for W8-1E15 is not capable of reaching the maximum before decreasing again because full depletion was not achieved. A difference between backside and topside biasing can be seen for W3-1E14 where the backside biased measurement performs better by about 0.2 µm.

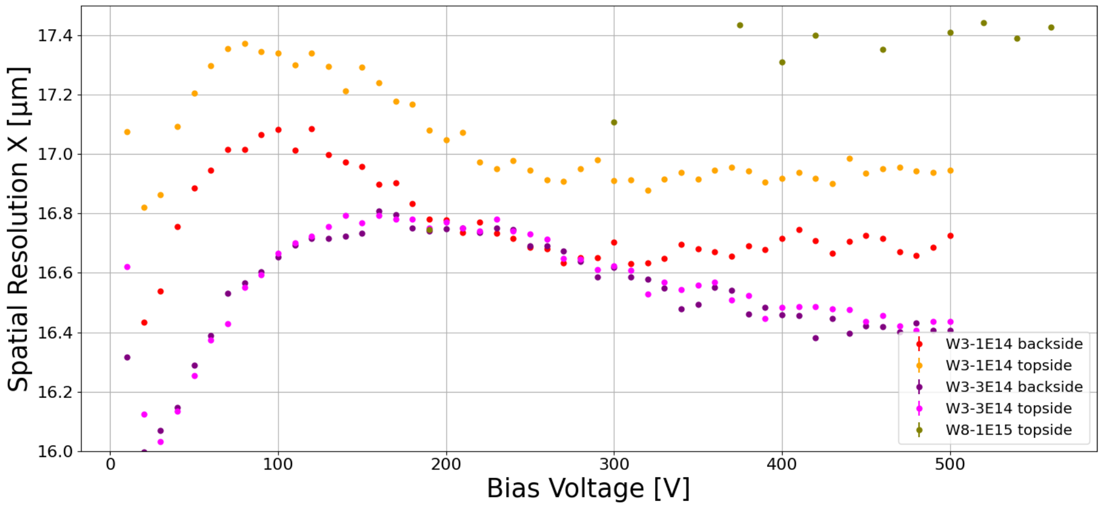

Figure 48: Spatial resolution of irradiated samples in X-direction as a function of bias voltage.

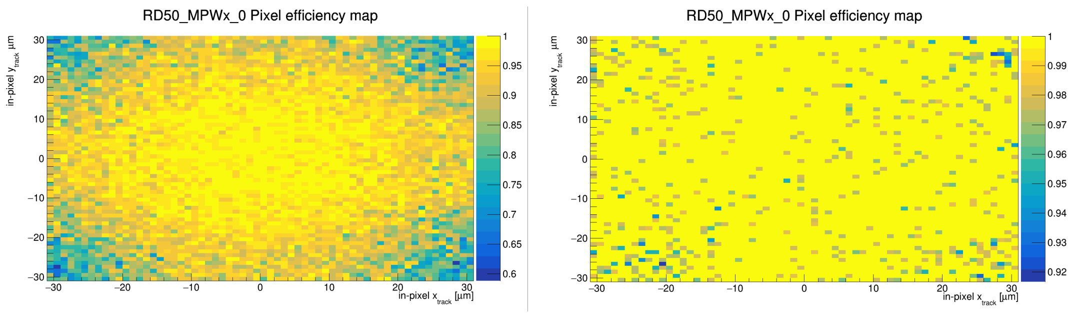

(a) Bias Voltage: 50 V

(b) Bias Voltage: 500 V

Figure 49: In-pixel efficiency for a bias voltage of a) 50 V and b) 500 V illustrating corner effects for an under depleted sensor (sample: W3-1E14).

4.3.3.5. Bias Voltage Characteristics

The numerical results of the bias voltage scans for the highest applied bias voltage settings are given in tab.8. For comparison, the results of the standard settings of W3-V from sec.4.2 are given as well.

Chip	Biasing	Bias Voltage [V]	ToT [LSB]	Cluster Size	σ_x [µm]
W3-V	backside	190	8.529 ± 0.005	1.368 ± 0.001	16.27
W3-1E14	topside	500	15.990 ± 0.010	1.187 ± 0.001	16.95
W3-1E14	backside	500	15.280 ± 0.009	1.192 ± 0.001	16.73
W3-3E14	topside	500	7.805 ± 0.006	1.252 ± 0.001	16.44
W3-3E14	backside	500	7.739 ± 0.005	1.250 ± 0.001	16.41
W8-1E15	topside	560	2.675 ± 0.038	1.064 ± 0.003	17.43

Table 8: Comparison of measured parameters for different fluences and bias voltages.

4.3.3.6. Timing

The time resolution was evaluated as described in sec.4.2.5 by means of a rms truncated to the innermost 99 % of the distribution. No manual time shift had to be applied in the analysis due to a correctly set *CONF_REG_ TS_ CTRL register*. An example of the unprocessed time residuals is given in fig.50. The results are shown in fig.51. Because the time stamp for W8-1E15 was not working, its timing resolution could not be evaluated.

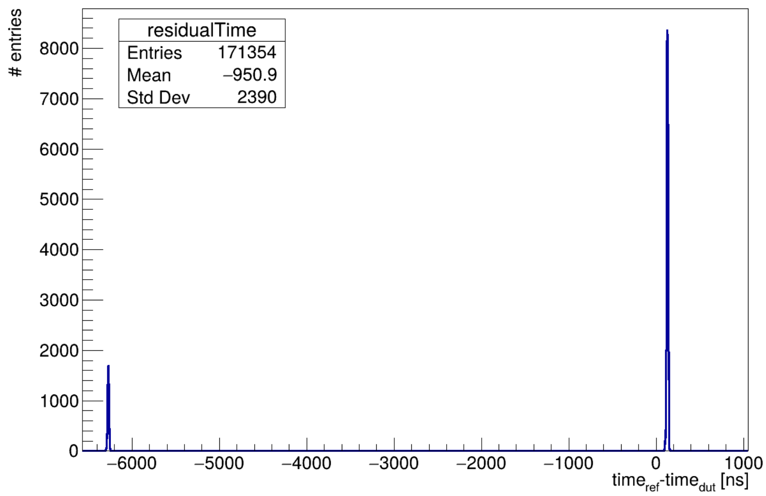

Figure 50: Example time residuals for the sample W3-1E14 operated at −180 V bias voltage.

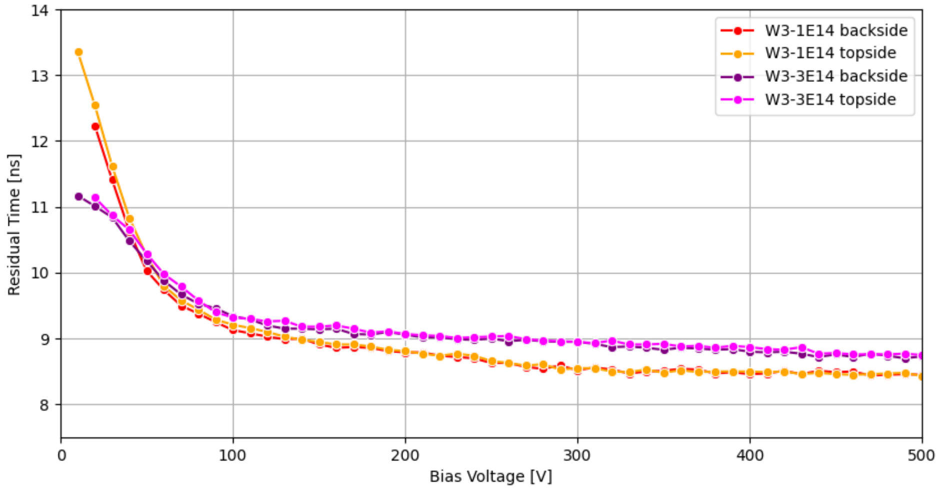

Figure 51: Time residuals of irradiated samples for increasing bias voltage.

The sample W3-1E14 shows the best timing resolution of 8.45 ns at 500 V bias voltage followed by W3-3E14 with a resolution of 8.7 ns. All samples show an improvement of the timing resolution with increasing bias voltage. The beneficial contribution also continues above the full depletion voltage. No evident difference in the performance with backside or topside biasing could be observed.

4.3.4. VNFB DAC Scans with Irradiated Samples

The impact of the VNFB setting was tested with three measurements of two samples. For W3-1E14, a measurement was done for forward and backside biasing with 190 V and a threshold of 200 mV. W3-3E14 was tested with a higher bias voltage of 400 V and a lower threshold of 50 mV. The VNFB settings were changed from zero to 50 in steps of ten. A direct comparison between a VNFB value of 20, which is close to the nominal value of 18, and the highest measured VNFB value of 50 is shown in tab.9 for W3-1E14 with backside biasing. Given uncertainties for mean values refer to the standard error. The ToT can be increased by 73.5 %, the cluster size by 0.9 % and the spatial resolution by about 1.3 %. Also the efficiency can be improved by about 0.26 %.

W3-1E14	VNFB: 20	VNFB: 50
ToT [LSB]	13.140 ± 0.008	22.810 ± 0.015
Cluster Size	1.147 ± 0.001	1.158 ± 0.001
Spatial Res. X [µm]	16.84	16.62
Efficiency [%]	99.48	99.74

Table 9: Comparison of performance of W3-1E14 with backside biasing with tuned VNFB compared to a setting close to the nominal setting.

4.3.4.1. ToT

As shown in fig.52, the ToT increases from 13.14 LSB (VNFB = 20) to 22.80 LSB (VNFB = 50) for W3-1E14 with backside biasing. Only a minor differences of 0.31 LSB can be observed between backside and topside biasing for a VNFB of 50. The ToT of W3-3E14 shows an increase only till a VNFB of 30 and decreases again for higher values. The lower threshold used for this sample leads to a peak at low ToT times (see fig.53) and shifts the average to lower values.

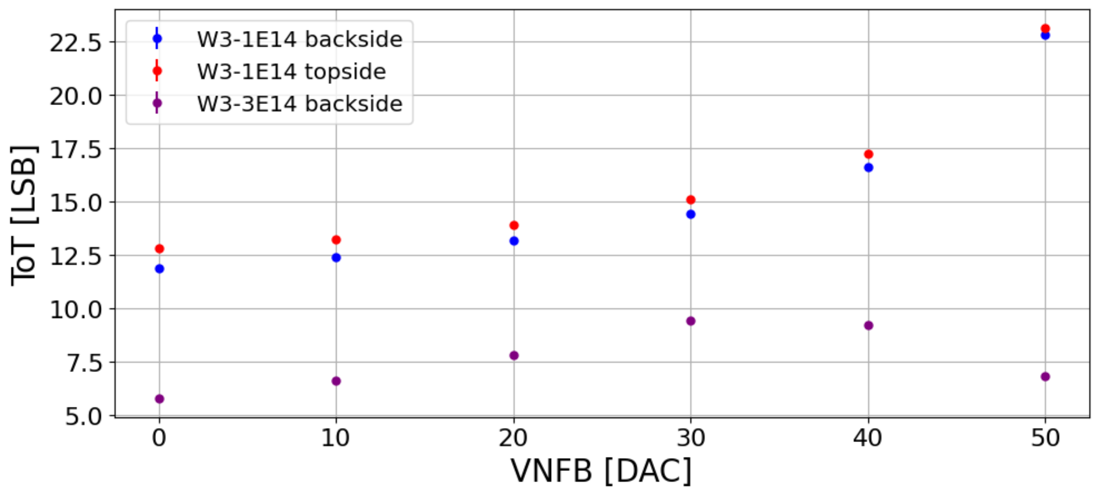

Figure 52: ToT versus VNFB for irradiated samples.

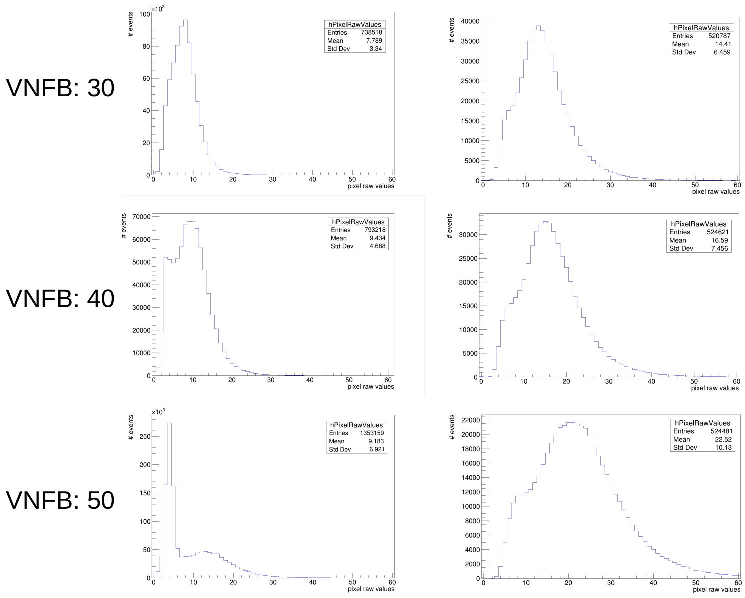

Figure 53: Evolution of the ToT distribution with changing VNFB for W3-3E14 (left) and W3-1E14 (right) biased from the back.

4.3.4.2. Cluster Size

The cluster size shows a similar behavior as the ToT. As shown by fig.54, the cluster size of the sample W3-1E14 increases slightly with only minor differences between backside and topside biasing while for W3-3E14, it increases only until a VNFB setting of 30.

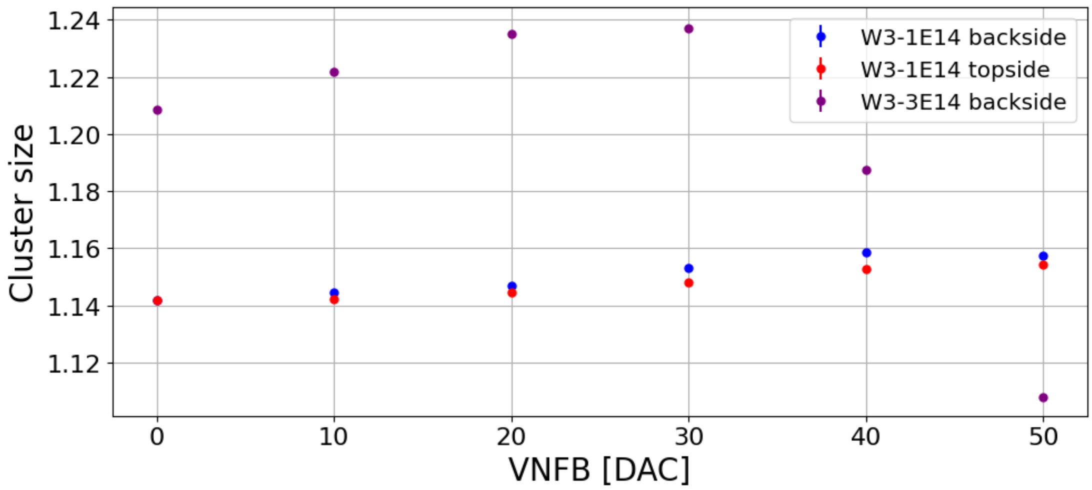

Figure 54: Cluster size versus VNFB for irradiated samples.

4.3.4.3. Spatial resolution

The spatial resolution improves with higher VNFB values as shown in fig.55. Compared to the nominal setting, it improves by about 1.3 % at a VNFB setting of 50 for W3-1E14. For W3-3E14, an improvement of 1.5 % from 16.46 µm to 16.21 µm can be observed. Although an improvement of the spatial resolution could be measured, its impact is too low for a relevant improvement of the performance of the chip. The better performance of the sample irradiated to a higher fluence of $3 \times 10^{15}\,\mathrm{n_{eq}cm^{-2}}$ results from the operation at a higher bias voltage of 400 V.

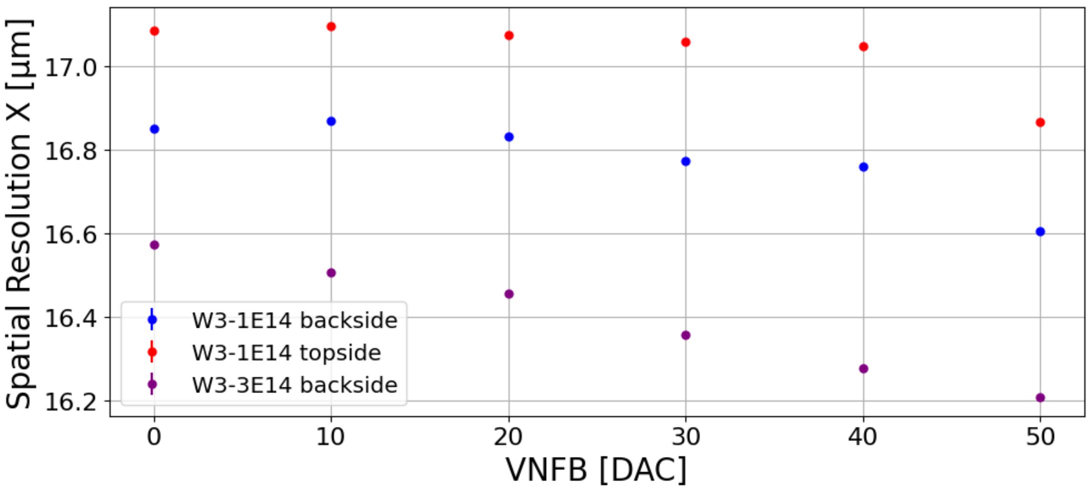

Figure 55: Spatial resolution versus VNFB for irradiated samples.

5. TJ-Monopix2

5.1. Lab Measurements

The data presented in this section was collected in June and July 2024 at the laboratories at HEPHY. The power consumption measurements were done in order to estimate design parameters for the OBELIX [9] chip. The temperature calibration was done as preparation for a test beam at DESY in July 2024 (see sec.5.2.4).

5.1.1. Power Consumption Measurements

For the power consumption measurements, the current for a given supply voltage of the four inputs of the TJ-Monopix2 were measured with a HAMEG HMP4040 [34]. The VPC was directly measured on the pins of the PCB using a multimeter. The chip was operated in a closed box in order to avoid light. For all measurements, the current of all four inputs was recorded.

5.1.1.1. Clock frequency and BCID

The power consumption of the periphery depends linearly on the clock frequency as shown in fig.56 as expected for CMOS digital circuitries. For the measurement, the sample W08R19 with 411 active columns was used with 6 V applied to PWELL. The naming of the samples corresponds to the wafer number they are produced of (WXX) and the position (RXX) on them. With enabled BCID, the VDDP increases with 4.728 mA/MHz while with disabled BCID, the slope reduces to 0.584 mA/MHz. The power consumption of the other three power domains of the chip do not depend on the clock frequency.

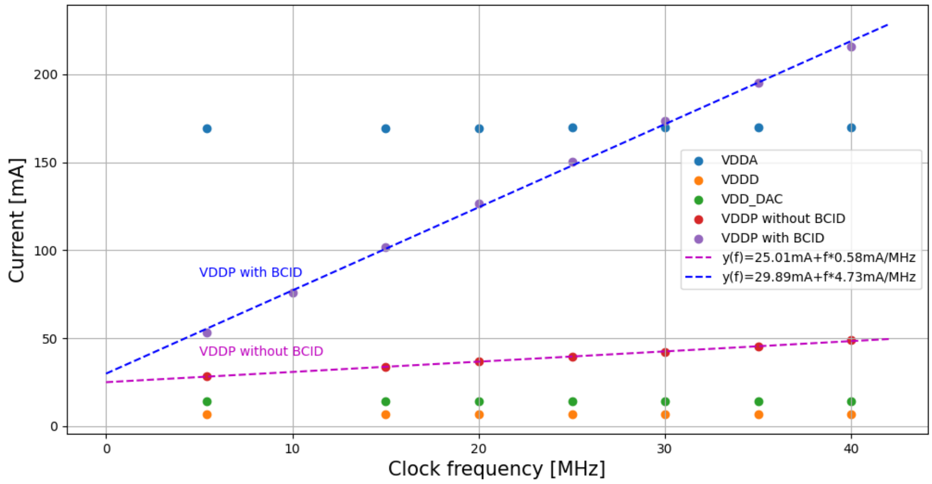

Figure 56: Impact of the clock frequency on VDDP with and without BCID.

The difference between the current with enabled and disabled BCID I_{diff} allows to calculate the total capacitance C of the wires distributing the BCID over the 256 double columns. In eq.32, the calculation is shown for a single double column C_l at the standard clock frequency of 40 MHz.

$$C_l = \frac{I_{diff}}{fU \times 256} \approx \frac{165.76\,\mathrm{mA}}{40\,\mathrm{MHz} \times 1.8\,\mathrm{V} \times 256} \approx 8.9\,\mathrm{pF} \tag{32}$$

5.1.1.2. IBIAS

The power consumption of the analog part of the matrix is influenced by the applied bias current to the first amplifier stage in each pixel, IBIAS (see fig.24), as depicted in fig.57. For the measurement, a bias voltage of 10 V was applied and 16 active columns were used. The default value of IBIAS is 100 DAC which corresponds to 550 nA/pixel. A linear fit of VDDA results in an offset of 14.83 mA and an increase of 1.58 mA/DAC. With a measured current of 173.2 mA for an IBIAS of 100 DAC, the contribution of IBIAS to VDDA is about 91 %.

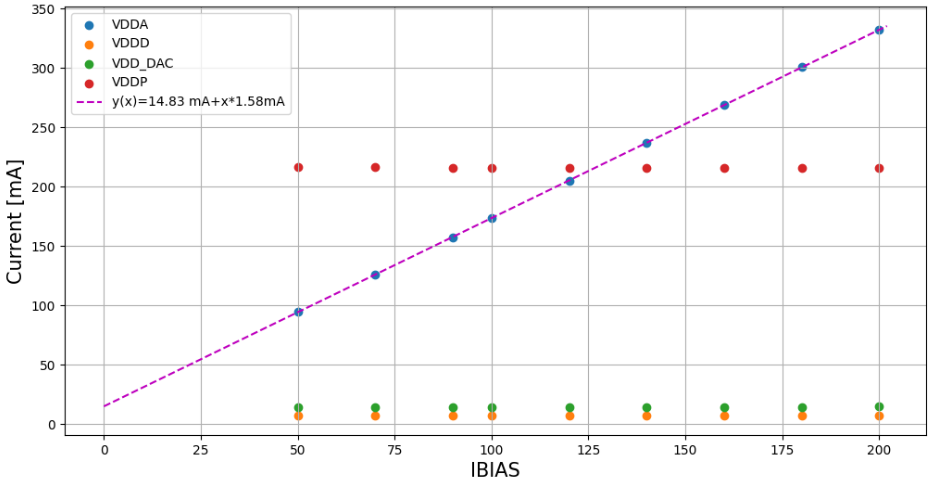

Figure 57: Impact of IBIAS on VDDA.

5.1.1.3. Occupancy and VPC

The pre-charge current I_VPC depends on the set VPC as well as on the hit rate. In order to generate different hit rates in the laboratory, the effective threshold was changed by the DAC settings to generate noise hits. With this procedure, the impact of the hit rate was measured for three different VPC settings, as shown in tab.10 and fig.58. For the measurements, the sample W08R19 was used with 100 active columns and 100 active rows and an applied potential of 6 V to PWELL. The noise hits were measured for 10 seconds for each measurement.

VPC [V]	**Δ I_VPC [μA/MHz]**	**I_VPC(0) [μA]**
1.61	52	3333
1.74	62	2627
1.79	70	3953

Table 10: Fit parameters for the impact of the hit rate on I_VPC for three different VPC settings.

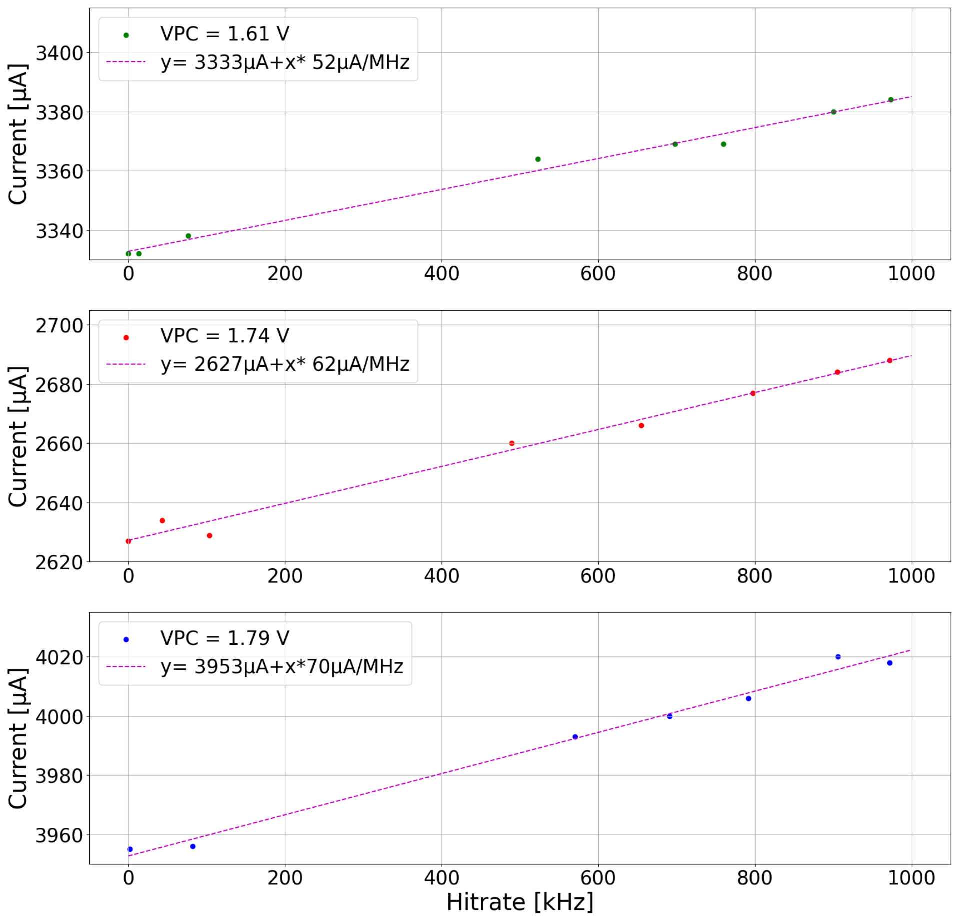

Figure 58: I_VPC measurements using hits generated by noise.

5.1.2. Temperature Calibration

The PCB of the Tj-Monopix2 features a Negative Temperature Coefficient Thermistor (NTC) for temperature measurements. Since the NTC has no direct contact to the chip, a calibration measurement is needed to calculate the actual temperature of the chip. For the calibration measurements, the thermocouple data logger TC-08 from Pico Technology [35] was used. Two temperature sensors were placed directly onto the chip matrix with thermal conductive tape as depicted in fig.59.

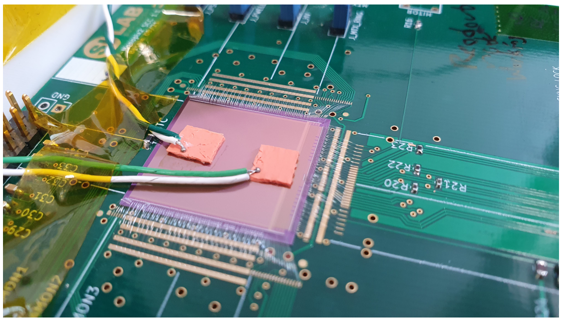

Figure 59: Setup for the temperature calibration measurements.

The ambient temperature throughout the measurements was 30 °C. For the NTC, the arithmetic mean of a 30 s long measurement was used in order to reduce noise. The temperature of the chip was increased by a heater which consists of four resistors placed at the backside of the PCB. With increasing current, the temperature of the resistors increases. In fig.60, a calibration curve for both temperature sensors is shown. The mean of the two curves, which is used as calibration curve, is shown in eq.33.

$$T_{chip} = -4.286°C + T_{NTC} \times 1.411 \tag{33}$$

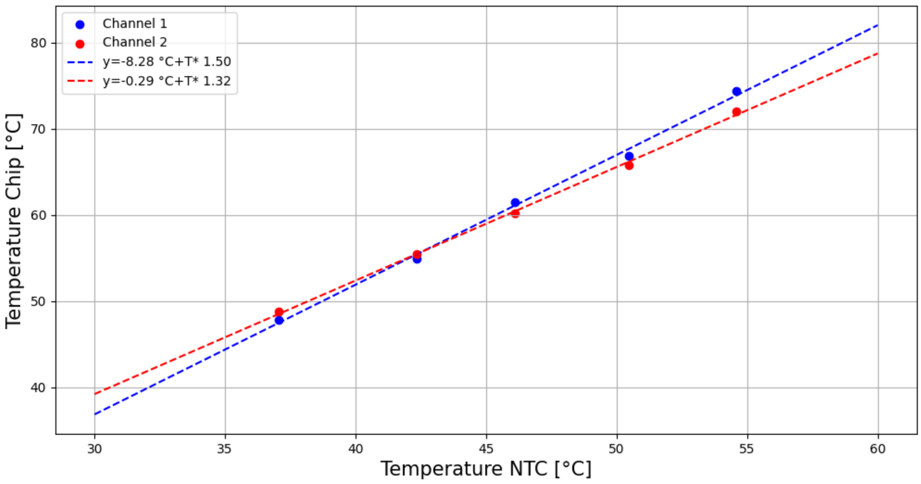

Figure 60: Calibration curve from the NTC temperature to the temperature of the chip.

5.2. Efficiency and Performance Measurements

The data presented in this section was collected throughout a test beam at the test beam facility at DESY [29] in July 2024. An unirradiated sample (W02R05) and a proton irradiated sample (W08R06) were measured. W08R06 was irradiated with protons to a fluence of $5 \times 10^{14}\,\mathrm{n_{eq}cm^{-2}}$ at CYRCé [36]. The analysis done throughout this thesis is preliminarily and can slightly differ from the final results presented by the Belle II collaboration.

5.2.1. Test Beam Setup

As beam telescope, the DURANTA telescope provided by the test beam facility was used. It consists of six planes of MIMOSA26 MAPS with a pixel size of 18.4 µm × 18.4 µm arranged in 1152 columns and 576 rows. The intrinsic resolution of the sensors is 3.24 ± 0.09 µm allowing a track resolution up to 1.83 ± 0.03 µm. Triggering is done by two additional scintillators in combination with a TLU. [29]

The TJ-Monopix2 was mounted as DUT on a 3D printed bracket with a heater mounted on the backside of the chip as depicted in fig.61. As DAQ, the BDAQ53 [37] was used. For the communication and data storage between the different components during data taking, the data acquisition software framework EUDAQ2 [27] was used.

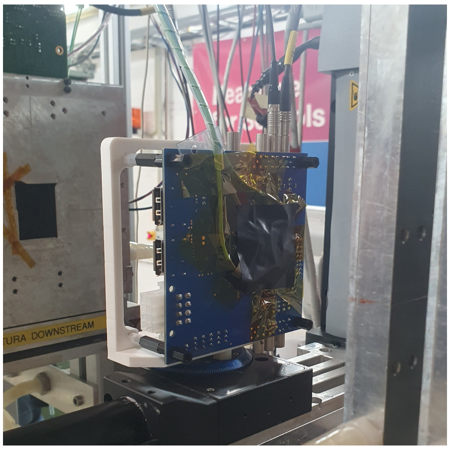

Figure 61: TJ-Monoopix2 mounted as DUT in the DURANTA telescope with attached heater.

5.2.2. Performance without Irradiation

This section contains data from the HVC and DCC front end of the unirradiated sample W02R05. In tab.11, the settings and results of two statistic runs are shown. Due to the lower threshold used for the HVC front end, its mean ToT of 45.35 LSB is higher than the one of the DCC front end with 27 LSB. The deviations given for the mean values refer to one standard deviation of the whole data set.

W02R05	**HVC front end**	**DCC front end**
Bias Voltage [V]	20	6
Threshold [DAC]	18.8	29.50
ToT [LSB]	45.35	27.00
Cluster Size	1.462	1.527
Spatial Res. X/Y [µm]	9.35/10.23	9.82/10.67
Efficiency [%]	99.94	99.93

Table 11: Performance of the HVC and DCC front end of the unirradiated sample W02R05.

Both ToT distributions depicted in fig.62 show a pronounced double peak due to charge sharing. The cut of the distributions at a value of 128 results from the limiting 7 bit timestamp enabling 2^7 (128) values.

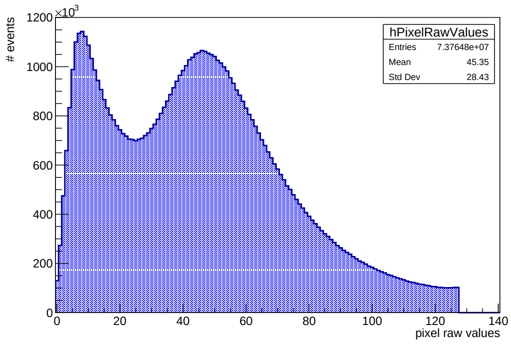

(a) HVC front end

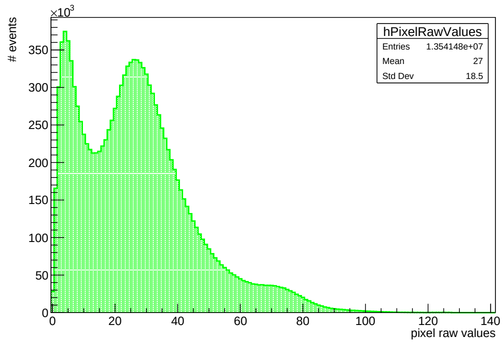

(b) DDC front end

Figure 62: ToT distribution for unirradiated TJ-Monopix2 for a) HVC and b) DCC front end.

5.2.3. Impact of Proton Irradiation

The impact of proton irradiation on the two cascode front ends of the sample W08R06 is shown in tab.12. The bias voltage was increased and the effective threshold remained in the same range compared to the unirradiated sample. The HVC front end could only be operated up to an efficiency of 97.68 % while the DCC front end still achieved an efficiency of 99.56 %. The cluster size is reduced for both front ends. The irradiation also has a negative impact on the spatial resolution.

W08R06	**HVC front end**	**DCC front end**
Bias Voltage [V]	30	20
Threshold [DAC]	18.0	30.6
ToT [LSB]	6.529	5.169
Cluster Size	1.232	1.207
Spatial Res. X/Y [µm]	10.77/10.79	10.58/11.03
Efficiency [%]	97.68	99.56

Table 12: Performance of the HVC and DCC front end of the proton irradiated sample W08R06.

The mean values of the ToT distributions reduces from 45.35 to 6.529 LSB for the HVC front end and from 27 to 5.169 LSB for the DCC front end. In fig.63, the corresponding distributions are shown. For the HVC front end, no separate charge sharing peak is visible.

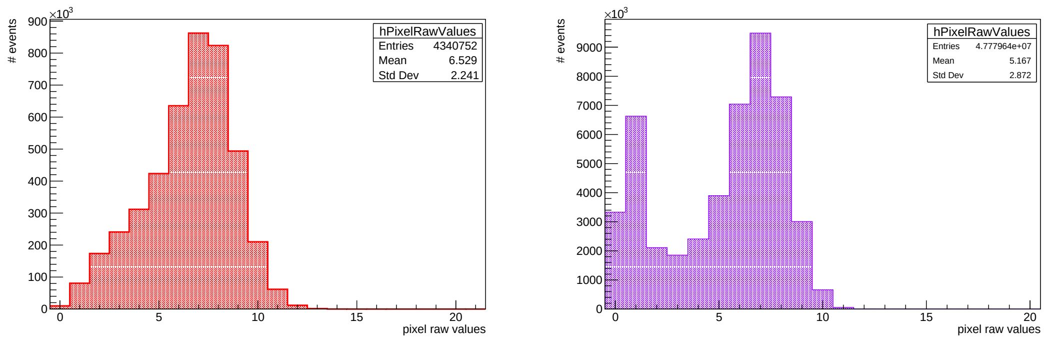

(a) HVC front end   (b) DCC front end

Figure 63: ToT distribution for proton irradiated TJ-Monopix2 for a) HVC and b) DDC front end.

5.2.4. Temperature measurements

In order to observe the impact of increasing temperature on the TJ-Monopix2, its performance was measured for five different temperatures. The measurements were done with the HVC front end at a bias voltage of 30 V of the proton irradiated sample W08R06. The DAC settings were adjusted to each temperature, resulting in different effective thresholds given in tab.13 together with the results. The temperature was measured with the NTC on the PCB which allows calculating the chip temperature according to the calibration from eq.33.

T_{NTC} [°C]	T_{Chip} [°C]	Threshold [DAC]	Spatial Res. X/Y [µm]	ε [%]
35	45.1	27.6	9.45/9.61	85.46
36	46.5	28.5	9.37/9.31	77.00
37	49.0	28.7	9.30/9.28	73.19
39	50.7	32.7	9.18/9.17	72.19
45	59.2	42.8	9.11/9.06	60.27

Table 13: Spatial resolution and efficiency of the TJ-Monopix2 for different temperatures of the HVC front end.

For a chip temperature of 45.1 °C, only an efficiency of 85.46 % instead of 97.68 % at room temperature (see tab.12) can be achieved. The efficiency decreases with increasing temperature, as shown in fig.64. However, the temperature seems not to have a negative effect on the spatial resolution.

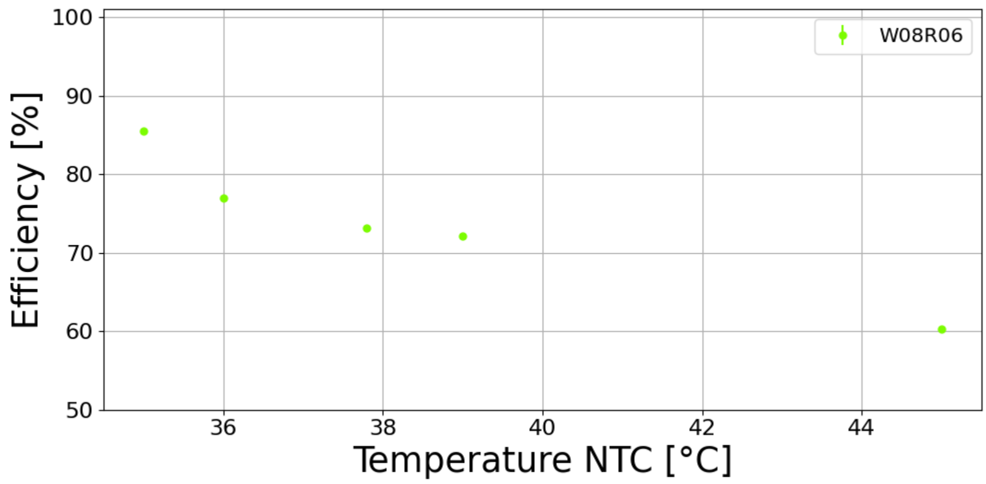

Figure 64: Efficiency of the TJ-Monopix2 for different temperatures.

The efficiency loss occurs due to the higher effective threshold which is needed to cope with noise resulting from the increased temperature. Due to the higher threshold, only hits close to the collection electrode are detected. This behavior is illustrated in fig.66 which shows the in pixel efficiency for two measurements. Because of this, the cluster size approaches to one (see fig.65) since charge sharing can hardly be measured and the spatial resolution improves slightly due to not detected hits with further distance to the collection electrode.

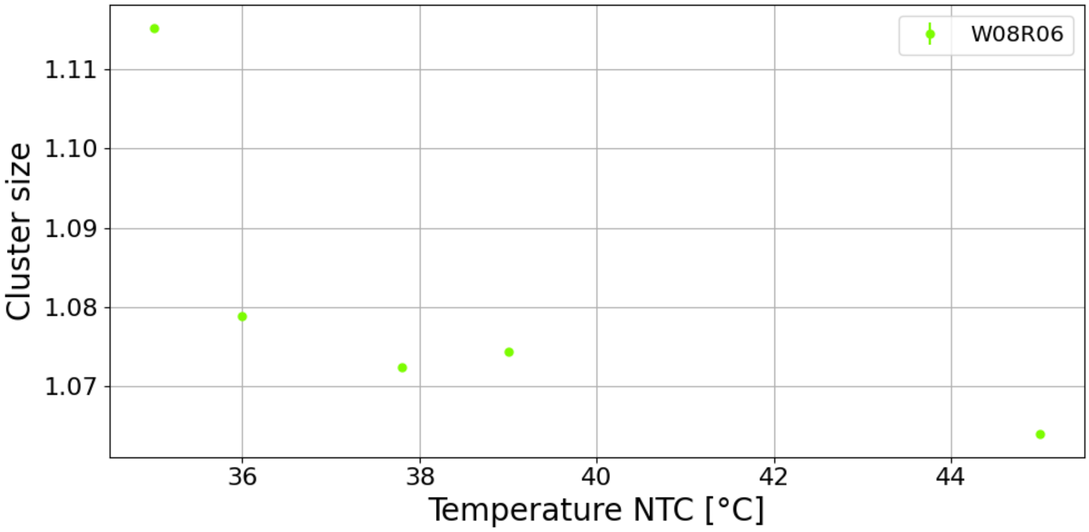

Figure 65: Cluster size of the TJ-Monopix2 for different temperatures.

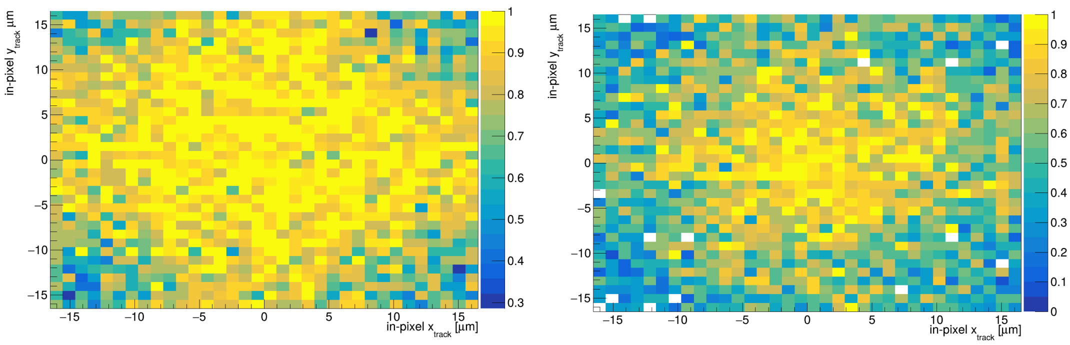

(a) thr: 27.6 DAC, T: 45.1 °C

(b) thr: 59.2 DAC, T: 59.2 °C

Figure 66: In-pixel efficiencies for different effective thresholds and temperatures illustrating corner effects

6. Operation Settings

This chapter summarizes the achieved spatial resolution and efficiencies together with the used operation settings. In tab.14, operation settings together with the spatial resolution and efficiency for each fluence from chapter 4 are summarized. In tab.15, the settings and results for the performance measurements of the TJ-Monopix2 from chapter 5 are given.

Sample	**Fluence**	**Bias Voltage**	**Threshold**	**Spatial Res.**	**Efficiency**
	[$n_{eq}cm^{-2}$]	[V]	[mV]	X/Y [µm]	[%]
W3-V	0	190	40	16.27/16.32	99.99
W3-1E14	1×10^{14}	500	200	16.73/ 16.58	99.66
W3-3E14	3×10^{14}	500	50	16.41/16.17	99.55
W8-1E15	1×10^{15}	560	70	17.43/16.60	98.27

Table 14: Operation settings and performance for measured RD50-MPW4 samples.

Sample	**Fluence**	**Bias Voltage**	**Threshold**	**Spatial Res.**	**Efficiency**
	[$n_{eq}cm^{-2}$]	[V]	[DAC]	X/Y [µm]	[%]
W02R05 HVC	0	20	18.8	9.35/10.23	99.94
W02R05 DCC	0	-6	29.5	9.82/10.67	99.93
W08R06 HVC	5×10^{14}	30	18.0	10.77/10.79	97.68
W08R06 DCC	5×10^{14}	-20	30.6	10.58/11.03	99.56

Table 15: Operation settings and performance for measured TJ-Monopix2 samples.

The comparison of the results outlines the differences between the two chips. The spatial resolution of the TJ-Monopix2, which follows the small collection electrode design approach, is better due to its smaller pixel size of 33.04 µm × 33.04 µm compared to the RD50-MPW4 with a pixel size of 62 µm × 62 µm following the large collection electrode design approach. When comparing the radiation hardness of the chips, the HV-CMOS approach seems to work out better for the RD50-MPW4 since only an efficiency of 97.68 % could be reached for the HVC front end of the TJ-Monopix2. However, the DCC front end still performed well at a fluence of $5 \times 10^{14}\, n_{eq}cm^{-2}$.

7. Conclusion

7.1. RD50-MPW4

Within this thesis, the performance of the RD50-MPW4 could be characterized by test beam results of three test beams. For four unirradiated samples, an efficiency above 99.9 % for an applied bias voltage of 190 V could be measured. Their average spatial resolution is 16.70 ± 1.05 µm in X and 16.90 ± 1.34 µm in Y direction compared to a spatial resolution of 17.90 µm calculated from the pixel pitch without taking charge weighting into account. By scanning the performance for different bias voltages, the full depletion of the RD50-MPW4 without irradiation could be shown to be around 190 V. Up to a threshold of 185 mV, all samples performed with an efficiency above 99.9 %. No evident difference could be observed for backside processed samples due to a lack of samples. For the analysis of timing, the overflow counter had to be taken into account. By only evaluating events with correct time stamps, an average timing resolution of 9 ns could be observed for the RD50-MPW4. By increasing the DAC settings for the VNFB, the cluster size and ToT could be increased, leading to a beneficial effect on the spatial resolution and efficiency. However, the impact is too small in order to improve the performance of the chip. The upper limit for the VNFB setting could be shown to be between 50 and 60 DAC.
For the performance measurements with radiation damage, four irradiated samples irradiated to different fluences were measured. Up to a fluence of $3 \times 10^{14}\,\mathrm{n_{eq}cm^{-2}}$, an efficiency above 99 % could be reached. For a fluence of $1 \times 10^{15}\,\mathrm{n_{eq}cm^{-2}}$, an efficiency of 98.27 % could be measured before it broke down. With increasing irradiation of the samples, more bias voltage was needed in order to achieve good efficiencies. For the spatial resolution, no negative impact from the irradiation could be observed. For the timing performance, only a slight difference of 0.25 ns could be measured between the samples W3-1E14 and W3-3E14. Biasing from the front or back has no impact on the timing performance. Good performance could be shown for a sample irradiated to a fluence of $1 \times 10^{15}\,\mathrm{n_{eq}cm^{-2}}$.
For a better understanding of the impact of irradiation on the chip performance in the region above $1 \times 10^{15}\,\mathrm{n_{eq}cm^{-2}}$, further measurements have to be conducted with more samples irradiated in the range between $1 \times 10^{15}\,\mathrm{n_{eq}cm^{-2}}$ and $1 \times 10^{16}\,\mathrm{n_{eq}cm^{-2}}$. Furthermore, the increased ToT of 16 LSB of the sample W3-1E14 compared to the average ToT of 7.84 ± 0.72 LSB of the unirradiated samples remains unclear.

7.2. TJ-Monopix2

Design parameters could be evaluated for the TJ-Monopix2 from laboratory measurements. Furthermore, a calibration for temperature measurements of the surface of the chip could be done. For an unirradiated sample, the HVC front end could be operated with an efficiency of 99.9 % and a spatial resolution of 9.35 µm in X and 10.23 µm in Y direction, which is in the expected range compared to a spatial resolution of 9.54 µm calculated from the pixel pitch. For the DCC front end, an efficiency of 99.9 % and a spatial resolution of 9.82 µm (X) and 10.67 µm (Y) could be achieved. With a proton irradiated sample irradiated to a fluence of $5 \times 10^{14}\,\mathrm{n_{eq}cm^{-2}}$, the efficiency reduced to 97.6 % for the HVC and to 99.5 % for the DCC front end. The spacial resolution increased slightly to 10.77/10.79 µm (HVC) and 10.58/11.03 µm (DCC). A negative impact of high ambient temperature could be shown for the HVC front end of the TJ-Monopix2. At a chip temperature of 45.1 °C, the efficiency is already reduced to 85.46 %.
For a better characterization of the radiation hardness of the TJ-Monopix2, further fluences have to be tested. For better control over the temperature, a modified temperature control system is needed for a better characterization of the impact of the temperature on the chip performance. Measurements are planned in a temperature range between 10 and 40 °C.

References

[1] I. Adachi, T. Browder, P. Križan, S. Tanaka, Y. Ushiroda, B. I. Collaboration, *et al.*, "Detectors for extreme luminosity: Belle II," *Nuclear Instruments and Methods in Physics Research Section A: Accelerators, Spectrometers, Detectors and Associated Equipment*, vol. 907, pp. 46–59, 2018.

[2] `https://rd50.web.cern.ch/` [Accessed: 10.12.2024].

[3] M. Thomson, *Modern particle physics.* Cambridge University Press, 2013.

[4] G. Viehhauser and T. Weidberg, *Detectors in Particle Physics: A Modern Introduction.* Taylor & Francis, 2024.

[5] R. Frühwirth and A. Strandlie, *Pattern Recognition, Tracking and Vertex Reconstruction in Particle Detectors.* Springer Nature, 2021.

[6] H. Kolanoski and N. Wermes, *Particle Detectors: Fundamentals and Applications.* Oxford University Press, 06 2020.

[7] K. Akai, K. Furukawa, H. Koiso, *et al.*, "Superkekb collider," *Nuclear Instruments and Methods in Physics Research Section A: Accelerators, Spectrometers, Detectors and Associated Equipment*, vol. 907, pp. 188–199, 2018.

[8] P. Branchini, "The Belle II Experiment: Status and Prospects," *Universe*, vol. 4, no. 10, p. 101, 2018.

[9] M. Babeluk, D. Auguste, M. Barbero, P. Barrillon, J. Baudot, T. Bergauer, F. Bernlochner, G. Bertolone, C. Bespin, S. Bettarini, *et al.*, "The OBELIX chip for the Belle II VTX upgrade," *Nuclear Instruments and Methods in Physics Research Section A: Accelerators, Spectrometers, Detectors and Associated Equipment*, vol. 1067, p. 169659, 2024.

[10] H. Aihara, A. Aloisio, D. Auguste, M. Aversano, M. Babeluk, S. Bahinipati, S. Banerjee, M. Barbero, J. Baudot, A. Beaubien, *et al.*, "The Belle II Detector Upgrades Framework Conceptual Design Report," *arXiv preprint arXiv:2406.19421*, 2024.

[11] A. Colaleo, L. Ropelewski, K. Dehmelt, B. Liberti, M. Titov, J. Veloso, J. Monroe, A.-P. Colijn, A. Ereditato, I. G. Botella, *et al.*, *The 2021 ECFA detector research and development roadmap.* 2021.

[12] C. Zhang, B. Pilsl, S. Powell, E. Vilella, S. Zhang, T. Bergauer, R. Casanova, C. Irmler, U. Kraemer, R. Marco-Hernandez, *et al.*, "RD50-MPW: a series of monolithic High Voltage CMOS pixel chips with high granularity and towards high radiation tolerance," *Journal of Instrumentation*, vol. 19, no. 04, p. C04059, 2024.

[13] B. Pilsl, "Data acquisition systems for depleted monolithic active pixel sensors," 2022.

[14] K. Olive, "Review of particle physics," *Chinese Physics C*, vol. 38, p. 090001, aug 2014.

[15] G. Kramberger, V. Cindro, I. Mandić, M. Mikuž, and M. Zavrtanik, "Effective trapping time of electrons and holes in different silicon materials irradiated with neutrons, protons and pions," *Nuclear Instruments and Methods in Physics Research Section A: Accelerators, Spectrometers, Detectors and Associated Equipment*, vol. 481, no. 1-3, pp. 297–305, 2002.

[16] C. Bespin Valero, *Characterization of the TJ-Monopix2 Depleted Monolithic Active Pixel Sensor for High-Energy Physics Experiments.* PhD thesis, Universitäts-und Landesbibliothek Bonn, 2024.

[17] E. Bruun, *CMOS Analog IC Design: Fundamentals.* bookboon, 2022.

[18] I. Perić, L. Blanquart, G. Comes, P. Denes, K. Einsweiler, P. Fischer, E. Mandelli, and G. Meddeler, "The FEI3 readout chip for the ATLAS pixel detector," *Nuclear Instruments and Methods in Physics Research Section A: Accelerators, Spectrometers, Detectors and Associated Equipment*, vol. 565, no. 1, pp. 178–187, 2006.

[19] R. Casanova, C. Irmler, P. Sieberer, E. Vilella, C. Zhang, and S. Zhang, *RD50-MPW4 DOCUMENTATION.* RD50, 1st ed., June 2023.

[20] K. Moustakas, *Design and development of depleted monolithic active pixel sensors with small collection electrode for high-radiation applications.* PhD thesis, Bonn U., 2021.

[21] R. W. Doran, "The gray code," tech. rep., Citeseer, 2007.

[22] Y. Liu, C. Feng, I.-M. Gregor, A. Herkert, L. Huth, M. Stanitzki, Y. Teng, and C. Yang, "ADENIUM—A demonstrator for a next-generation beam telescope at DESY," *Journal of Instrumentation*, vol. 18, no. 06, p. P06025, 2023.

[23] G. Zhang, B. Nachman, S.-C. Hsu, and X. Chen, "The measurement of position resolution of RD53A pixel modules," *arXiv preprint arXiv:1908.10973*, 2019.

[24] S. Seidel, "Silicon strip and pixel detectors for particle physics experiments," *Physics Reports*, vol. 828, pp. 1–34, 2019.

[25] D. Dannheim, K. Dort, L. Huth, D. Hynds, I. Kremastiotis, J. Kröger, M. Munker, F. Pitters, P. Schütze, S. Spannagel, *et al.*, "Corryvreckan: a modular 4D track reconstruction and analysis software for test beam data," *Journal of Instrumentation*, vol. 16, no. 03, p. P03008, 2021.

[26] T. Vanat, "Caribou — A versatile data acquisition system," *PoS*, vol. TWEPP2019, p. 100, 2020.

[27] Y. Liu, M. Amjad, P. Baesso, D. Cussans, J. Dreyling-Eschweiler, R. Ete, I. Gregor, L. Huth, A. Irles, H. Jansen, K. Krueger, J. Kvasnicka, R. Peschke, E. Rossi, A. Rummler, F. Sefkow, M. Stanitzki, M. Wing, and M. Wu, "EUDAQ2—A flexible data acquisition software framework for common test beams," *Journal of Instrumentation*, vol. 14, p. P10033, oct 2019.

[28] P. Baesso, D. Cussans, and J. Goldstein, "The AIDA-2020 TLU: a flexible trigger logic unit for test beam facilities," *Journal of Instrumentation*, vol. 14, no. 09, p. P09019, 2019.

[29] R. Diener, J. Dreyling-Eschweiler, H. Ehrlichmann, I. Gregor, U. Kötz, U. Krämer, N. Meyners, N. Potylitsina-Kube, A. Schütz, P. Schütze, and M. Stanitzki, "The DESY II test beam facility," *Nuclear Instruments and Methods in Physics Research Section A: Accelerators, Spectrometers, Detectors and Associated Equipment*, vol. 922, pp. 265–286, 2019.

[30] H. Augustin, S. Dittmeier, J. Hammerich, A. Herkert, L. Huth, D. Immig, I. Perić, A. Schöning, A. Simancas, M. Stanitzki, and B. Weinläder, "TelePix – A fast region of interest trigger and timing layer for the EUDET Telescopes," *Nuclear Instruments and Methods in Physics Research Section A: Accelerators, Spectrometers, Detectors and Associated Equipment*, vol. 1048, p. 167947, 2023.

[31] F. Ulrich-Pur, L. Adler, T. Bergauer, A. Burker, A. De Franco, G. Guidoboni, A. Hirtl, C. Irmler, S. Kaser, S. Nowak, *et al.*, "Commissioning of low particle flux for proton beams at MedAustron," *Nuclear Instruments and Methods in Physics Research Section A: Accelerators, Spectrometers, Detectors and

Associated Equipment, vol. 1010, p. 165570, 2021.

[32] F. Ulrich-Pur, T. Bergauer, A. Burker, S. Hatamikia, A. Hirtl, C. Irmler, S. Kaser, P. Paulitsch, F. Pitters, and V. Teufelhart, "Imaging with protons at MedAustron," *Nuclear Instruments and Methods in Physics Research Section A: Accelerators, Spectrometers, Detectors and Associated Equipment*, vol. 978, p. 164407, 2020.

[33] B. Pilsl, T. Bergauer, R. Casanova, H. Handerkas, C. Irmler, U. Kraemer, R. Marco-Hernandez, J. M. de Cos, F. Palomo, S. Powell, *et al.*, "Characterization of the RD50-MPW4 HV-CMOS pixel sensor," *Nuclear Instruments and Methods in Physics Research Section A: Accelerators, Spectrometers, Detectors and Associated Equipment*, vol. 1069, p. 169839, 2024.

[34] `https://www.rohde-schwarz.com/ch/produkte/messtechnik/dc-netzgeraete/rs-hmp4000-netzgeraeteserie_63493-47360.html` [Accessed: 23.1.2025].

[35] `https://www.picotech.com/` [Accessed: 11.12.2024].

[36] `https://cyrce.fr/en/irradiation-2/` [Accessed: 12.12.2024].

[37] M. Daas, J. Dingfelder, T. Hemperek, J. Janssen, H. Krüger, D.-L. Pohl, M. Vogt, and N. Wermes, "BDAQ53, a Verification and Characterization Environment for the ATLAS Pixel Readout Chip RD53A," *Verhandlungen der Deutschen Physikalischen Gesellschaft*, 2018.

List of Figures

1. Schematic of a collider experiment and the interaction of different particle types with different detector systems. HCAL/ECAL: hadronic/electromagnetic calorimeter. [3] 1
2. Schematic overview of the detector systems of the Belle II experiment. [8] 3
3. Scheme of the concept of the cross section. $\dot{N}_R$ and $\dot{N}_{in}$ 5
4. Landau distribution as described in eq.3 for thin detectors [6]. . . . 6
5. Mean energy loss of charged pions in silicon showing the dependence on $\frac{1}{\beta^2}$ for low energies and $ln(\gamma) + const$ for higher energies. [6] . . . 8
6. Simulation of energy loss per path length for 100 MeV protons in water illustrating the Bragg peak. [6] 8
7. Illustration of the trajectory resulting from multiple Coulomb scattering and the deflection angle θ_{plane}. [14] 11
8. Conduction behavior of materials depending on the band gap E_G for insulators (a) semiconductors (b) and conductors (c,d). [6] . . . 12
9. Primitive cell of a diamond lattice (eg. Si). [6] 12
10. Model of a p-n junction. [4] 14
11. Possible new generated states due to impurities resulting from radiation damage in silicon. [4] 16
12. Full depletion voltage and effective charge carrier concentration as a function of the equivalent fluence illustrating type inversion. [6] . 18
13. a) Scheme of a strip detector and b) its utilization with two rotated planes for position measurements in two dimensions. 20
14. Scheme of the hybrid pixel detector approach separating the readout chip from the silicon sensor. [4] 21
15. Cross-section of a NMOS transistor. Metal connection to gate not depicted. [17] 22
16. Scheme of a CMOS device structure consisting of a PMOS and NMOS transistor. [17] 22
17. Scheme of the working principle of a MAPS [6] 23
18. Scheme of large collection electrode DMAPS. [6] 24
19. Scheme of the working principle of a small collection electrode DMAPS. [6] 25
20. Modified design approach for small collection electrode DMAPS. [6] 25
21. Block diagram of the RD50-MPW4. [19] 26
22. Block diagram of the in-pixel electronics of the RD50-MPW4. [19] . 27
23. Design of the different front-ends of the TJ-Monopix2. [16] 28

24. Schematic of the in-pixel analog amplifier circuit of the TJ-Monopix2 powered by V_{dd} (=VDDA). [20] 29
25. Scheme of a beam telescope consisting of 6 planes and a DUT. [22] 30
26. Scheme of the calculation of the ToT as the difference between the time stamps. 31
27. Correlation between two detector planes for correct alignment in x direction. 32
28. Illustration of the occurrence of clusters due to charge sharing. . . . 32
29. Illustration for the calculation of spatial residuals in one dimension for a single track. 33
30. Scheme of straight line fit and GBL fit for single particle tracking. . 36
31. Trade off between the spatial resolution normalized to the minimum value and efficiency depending on the applied relative cut for a given detector resolution of 17.898 µm in the geometry file. 40
32. Distributions for a) ToT and b) cluster size for W3-V. 41
33. Time over threshold versus bias voltage for four unirradiated samples. 42
34. Cluster size versus bias voltage for four unirradiated samples. 43
35. Efficiency versus threshold for four unirradiated samples. 44
36. Evaluation of truncated root mean square for spatial residuals. . . . 45
37. Time residuals of the RD50-MPW4 of the sample W8-V. 47
38. Residual times versus threshold for unirradiated samples. 48
39. Increase of cluster size and ToT with increasing VNFB in DAC units. 49
40. ToT distributions for selected VNFB settings. 49
41. Efficiency versus VNFB for W8-V. 50
42. Comparison of time residuals of a measurement with a VNFB of 50 (blue) and 60 (red) of W8-V. 51
43. Cooling setup for the RD50-MPW4 a) mounted in the beam telescope b) without DUT. 52
44. Efficiency maps for a) W3-3E14 and b)W8-1E15. 53
45. Efficiencies of the bias voltage scans with the irradiated samples. . . 54
46. ToT values of the bias voltage scans of irradiated samples. 54
47. Cluster sizes of the bias voltage scans of irradiated samples. 55
48. Spatial resolution of irradiated samples in X-direction as a function of bias voltage. 56
49. In-pixel efficiency for a bias voltage of a) 50 V and b) 500 V illustrating corner effects for an under depleted sensor (sample: W3-1E14). 56
50. Example time residuals for the sample W3-1E14 operated at −180 V bias voltage. 57
51. Time residuals of irradiated samples for increasing bias voltage. . . 58

52. ToT versus VNFB for irradiated samples. 59
53. Evolution of the ToT distribution with changing VNFB for W3-3E14 (left) and W3-1E14 (right) biased from the back. 60
54. Cluster size versus VNFB for irradiated samples. 61
55. Spatial resolution versus VNFB for irradiated samples. 62
56. Impact of the clock frequency on VDDP with and without BCID. . 64
57. Impact of IBIAS on VDDA. 65
58. I_VPC measurements using hits generated by noise. 66
59. Setup for the temperature calibration measurements. 67
60. Calibration curve from the NTC temperature to the temperature of the chip. 67
61. TJ-Monoopix2 mounted as DUT in the DURANTA telescope with attached heater. 68
62. ToT distribution for unirradiated TJ-Monopix2 for a) HVC and b) DCC front end. 69
63. ToT distribution for proton irradiated TJ-Monopix2 for a) HVC and b) DDC front end. 70
64. Efficiency of the TJ-Monopix2 for different temperatures. 71
65. Cluster size of the TJ-Monopix2 for different temperatures. 72
66. In-pixel efficiencies for different effective thresholds and temperatures illustrating corner effects 72

List of Tables

1. Bias voltages and default settings of the RD50-MPW4. [19] 27
2. Power supply channels of the TJ-Monopix2. 29
3. Overview of all measured samples. 38
4. Results of mean values for ToT and cluster size for standard settings (190V bias voltage) of unirradiated chips at room temperature. . . . 41
5. Minimum and maximum values for the measured bias voltage and threshold for unirradiated samples. 42
6. Results of the spatial resolution with truncated rms (99 %) for unirradiated chips operated with standard settings. 45
7. Threshold settings and scan ranges for bias voltage scans with irradiated samples. 53
8. Comparison of measured parameters for different fluences and bias voltages. 57
9. Comparison of performance of W3-1E14 with backside biasing with tuned VNFB compared to a setting close to the nominal setting. . . 59
10. Fit parameters for the impact of the hit rate on I_VPC for three different VPC settings. 65
11. Performance of the HVC and DCC front end of the unirradiated sample W02R05. 69
12. Performance of the HVC and DCC front end of the proton irradiated sample W08R06. 70
13. Spatial resolution and efficiency of the TJ-Monopix2 for different temperatures of the HVC front end. 71
14. Operation settings and performance for measured RD50-MPW4 samples. 73
15. Operation settings and performance for measured TJ-Monopix2 samples. 73

Acronyms

X_0 radiation length. 10

BCID bunch crossing ID. 29, 63, 64

CMOS Complementary Metal-Oxide-Semiconductors. 1, 4, 21, 22, 24, 26, 63

DAC digital-to-analog converter. 48, 53, 65, 71

DAQ data acquisition systems. 38, 45, 46, 68

DEPFET depleted p-channel field effect transistor. 3

DESY Deutsches Elektronen-Synchrotron. 38, 39, 41, 51, 63, 68

DMAPS monolithic active pixel sensor. 23, 27

DRDT detector R&D themes. 4

DSSDs Double-Sided Silicon micro-strip Detectors. 3, 39

DUT device under test. vi, 30, 33, 34, 36–40, 52, 68

GBL general broken line. 36

HEP high energy physics. 1, 3, 16

MAPS monolithic active pixel sensors. 21–23, 68

MIP minimum-ionizing particle. 7

NIEL non-ionizing energy loss. 16

NTC Negative Temperature Coefficient Thermistor. 66, 67, 71

OBELIX Optimised Belle II monolithic pixel. 4

PCB printed circuit board. 51, 52, 63, 66, 67, 71

PXD Pixel Detector. 3

rms root mean square. viii, 44, 45, 47, 57

SVD Silicon Vertex Detector. 3

TLU trigger logic unit. 35, 68

ToT time over threshold. vi, 27, 30, 31, 40–42, 48, 54, 58–60, 69, 70

TS-LE time stamp leading edge. 26, 27, 30

TS-TE time stamp trailing edge. 26, 27, 30

VXD Belle II vertex detector. 3, 4

A. Appendix

A.1. Corryvreckan detectors file

```
[Adenium_0]
coordinates = "cartesian"
material_budget = 0.00075
number_of_pixels = 1024, 512
orientation = -0.108346deg,0.310715deg,0.30172deg
orientation_mode = "xyz"
pixel_pitch = 29.24um,26.88um
position = -401.85um,-123.873um,0um
spatial_resolution = 8.441um,7.76um
time_resolution = 10us
type = "adenium"

[Adenium_1]
coordinates = "cartesian"
material_budget = 0.00075
number_of_pixels = 1024, 512
orientation = -2.54989deg,1.55335deg,-0.292839deg
orientation_mode = "xyz"
pixel_pitch = 29.24um,26.88um
position = 25.219um,301.29um,233mm
spatial_resolution = 8.441um,7.76um
time_resolution = 10us
type = "adenium"

[Adenium_2]
coordinates = "cartesian"
material_budget = 0.00075
number_of_pixels = 1024, 512
orientation = -2.65257deg,1.64869deg,-0.0671507deg
orientation_mode = "xyz"
pixel_pitch = 29.24um,26.88um
position = 7.174um,-2.193um,255mm
role = "reference"
spatial_resolution = 8.441um,7.76um
time_resolution = 10us
```

```
type = "adenium"

[RD50_MPWx_0]
coordinates = "cartesian"
material_budget = 0.0032
number_of_pixels = 64, 64
orientation = 0.344462deg,2.80325deg,90.421deg
orientation_mode = "xyz"
pixel_pitch = 62um,62um
position = -1.21207mm,826.397um,410mm
role = "dut"
spatial_resolution = 17.898um,17.898um
time_resolution = 50ns
type = "rd50_mpwx"

[Adenium_3]
coordinates = "cartesian"
material_budget = 0.00075
number_of_pixels = 1024, 512
orientation = -4.66783deg,3.00453deg,0.0495036deg
orientation_mode = "xyz"
pixel_pitch = 29.24um,26.88um
position = -655.317um,-248.713um,497mm
spatial_resolution = 8.441um,7.76um
time_resolution = 10us
type = "adenium"

[Adenium_4]
coordinates = "cartesian"
material_budget = 0.00075
number_of_pixels = 1024, 512
orientation = -4.96491deg,3.20106deg,0.0174179deg
orientation_mode = "xyz"
pixel_pitch = 29.24um,26.88um
position = -394.641um,8.498um,520mm
spatial_resolution = 8.441um,7.76um
time_resolution = 10us
type = "adenium"

[Adenium_5]
```

```
coordinates = "cartesian"
material_budget = 0.00075
number_of_pixels = 1024, 512
orientation = -5.01372deg,3.31622deg,-0.00870896deg
orientation_mode = "xyz"
pixel_pitch = 29.24um,26.88um
position = -490.583um,-165.008um,547mm
spatial_resolution = 8.441um,7.76um
time_resolution = 10us
type = "adenium"

[TLU_0]
coordinates = "cartesian"
orientation = 0.138197deg,0deg,55.3309deg
orientation_mode = "xyz"
position = -9.98549mm,-9.99mm,50000mm
role = "auxiliary"
time_resolution = 1ns
type = "tlu"
```

A.2. Corryvreckan config file

```
[Corryvreckan]
detectors_file = "<path_to_geo_file>"
histogram_file = "<name_of_outut_file>"
number_of_tracks = 50000
purge_output_directory = false


[EventLoaderEUDAQ2]
type = tlu
file_name = "<path_to_data>"
adjust_event_times=[["TluRawDataEvent", -10us, +10us]]

[EventLoaderEUDAQ2]
type = Adenium
file_name = "<path_to_data>"

[EventLoaderEUDAQ2]
#log_level = DEBUG
type = RD50_MPWx
name = RD50_MPWx_0
file_name = "<path_to_data>"
lsb_time = 25000
ts_mode = TLU

[Clustering4D]

[Tracking4D]
min_hits_on_track = 6
momentum = 4.2GeV
time_cut_abs = 2000s
exclude_dut = true
track_model = "gbl"


[DUTAssociation]
spatial_cut_rel = 5
time_cut_abs = 800000s
```

```
[AnalysisDUT]

[AnalysisEfficiency]
chi2ndof_cut = 3

[Correlations]

[AnalysisTiming]
name = "RD50_MPWx_0"
reference_type = "track"
time_range = 20us
time_binning = 5ns
cluster_charge_cut = 10000
```